Airborne Spectral Measurements of Ocean Directional Reflectance

CHARLES K. GATEBE

Goddard Earth Sciences and Technology Center, University of Maryland, Baltimore County, Baltimore, and NASA Goddard Space Flight Center, Greenbelt, Maryland

MICHAEL D. KING

NASA Goddard Space Flight Center, Greenbelt, Maryland

ALEXEI I. LYAPUSTIN

Goddard Earth Sciences and Technology Center, University of Maryland, Baltimore County, Baltimore, and NASA Goddard Space Flight Center, Greenbelt, Maryland

G. THOMAS ARNOLD

L-3 Communications Government Services, Inc., Vienna, Virginia, and NASA Goddard Space Flight Center, Greenbelt, Maryland

JENS REDEMANN

Bay Area Environmental Research Institute, Sonoma, and NASA Ames Research Center, Moffett Field, California

(Manuscript received 7 January 2004, in final form 7 June 2004)

ABSTRACT

The Cloud Absorption Radiometer (CAR) was flown aboard the University of Washington Convair 580 (CV-580) research aircraft during the Chesapeake Lighthouse and Aircraft Measurements for Satellites (CLAMS) field campaign and obtained measurements of bidirectional reflectance distribution function (BRDF) of the ocean in July and August 2001 under different illumination conditions with solar zenith angles ranging from 15° to 46°. The BRDF measurements were accompanied by concurrent measurements of atmospheric aerosol optical thickness and column water vapor above the airplane. The method of spherical harmonics with Cox–Munk wave-slope distribution is used in a new algorithm developed for this study to solve the atmosphere–ocean radiative transfer problem and to remove the effects of the atmosphere from airborne measurements. The algorithm retrieves simultaneously the wind speed and full ocean BRDF (sun's glitter and water-leaving radiance) from CAR measurements and evaluates total albedo and equivalent albedo for the water-leaving radiance outside the glitter. Results show good overall agreement with other measurements and theoretical simulations, with the anisotropy of the water-leaving radiance clearly seen. However, the water-leaving radiance does not show a strong dependence on solar zenith angle as suggested by some theoretical studies. The spectral albedo was found to vary from 4.1%–5.1% at $\lambda = 0.472$ μm to 2.4%–3.5% for $\lambda \geq 0.682$ μm. The equivalent water-leaving albedo ranges from 1.0%–2.4% at $\lambda = 0.472$ μm to 0.1%–0.6% for $\lambda = 0.682$ μm and 0.1%–0.3% for $\lambda = 0.870$ μm. Results of the validation of the Cox–Munk model under the conditions measured show that although the model reproduces the shape of sun's glitter on average with an accuracy of better than 30%, it underestimates the center of the sun's glitter reflectance by about 30% for low wind speeds (<2–3 m s^{-1}). In cases of high wind speed, the model with Gram–Charlier expansion seems to provide the best fit.

1. Introduction

In this study we discuss ocean surface anisotropy obtained with the National Aeronautics and Space Administration's (NASA) Cloud Absorption Radiometer (CAR) aboard the University of Washington Convair 580 (CV-580) research aircraft for different illumination conditions under clear sky. The measurements were obtained over the Atlantic Ocean off the eastern seaboard of the United States in the vicinity of the Chesapeake Light Tower and at nearby National Oceanic and Atmospheric Administration (NOAA) buoy stations (Fig. 1). Our study was part of the Chesapeake Lighthouse and Aircraft Measurements for Satellites (CLAMS) field experiment that took place between 10 July and 2 August 2001.

Corresponding author address: Dr. Charles K. Gatebe, Goddard Earth Sciences and Technology Center, University of Maryland, Baltimore County, Baltimore, MD 21228-5398.
E-mail: gatebe@climate.gsfc.nasa.gov

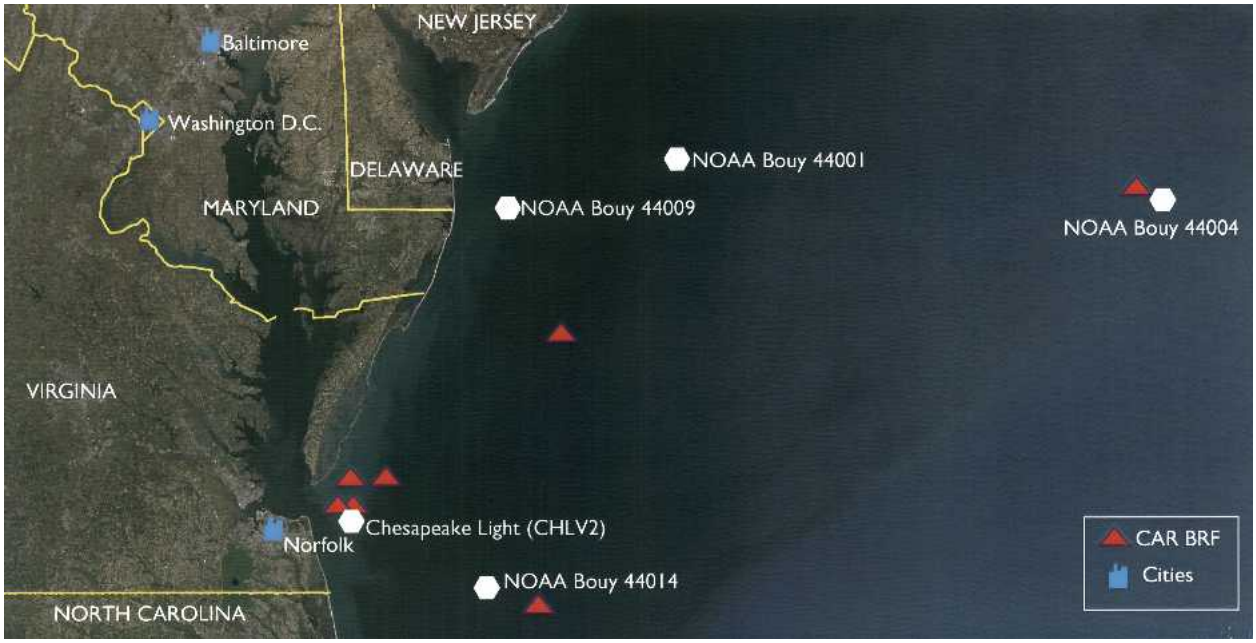

FIG. 1. Locations of airborne measurements of BRDF obtained during the CLAMS field experiment from 10 Jul to 2 Aug 2001 using NASA's CAR. On four flight days (10, 17, and 30 Jul and 2 Aug), measurements were taken in the vicinity of Chesapeake Light, on 23 Jul closer to buoy 44009, on 26 Jul in the vicinity of buoy 44014, and on 31 Jul in the vicinity of buoy 44004. The background image on which the BRDF locations are mapped is a true color composite of MODIS from *Terra* acquired on 13 Apr 2003.

The ocean radiance field beneath the surface is generally not isotropic. This has been shown in simulation studies of radiation transport within the ocean–atmosphere system using Monte Carlo methods (Morel and Gentili 1993, 1996; Morel et al. 1995). This anisotropy results from the anisotropic optical properties of the water body (namely, its volume scattering function) combined with the illumination conditions that prevail above the surface (Morel and Gentili 1993). Results from field measurements of upwelling radiance distribution at several wavelengths using a submersible camera system confirm the anisotropic nature of the ocean radiance field just beneath the water surface (Morel et al. 1995). However, there seem to be only a few reported measurements, especially at an aircraft altitude, to validate the bidirectional structure of the radiance field leaving the ocean surface over a given scene. We are only aware of the study by Soulen et al. (2000), which discusses spectral bidirectional reflectance distribution functions (BRDFs) of the ocean–atmosphere system from measurements obtained over the Atlantic Ocean and Persian Gulf from an aircraft. This study, however, missed the details of the bidirectional structure of the radiance field just above the ocean surface because of a lack of atmospheric correction. The anisotropy of the radiance field just above the ocean surface has practical consequences for the interpretation of the ocean signal detected remotely either by aircraft or satellite-borne radiometers and affects retrieved products such as ocean color and aerosols. For example, a theoretical study by Yang and Gordon (1997) shows that the error in water-leaving radiance caused by assuming the upwelling radiance beneath the ocean surface to be reflected uniformly in all directions is significant in comparison to other errors expected in the water-leaving radiance. This effect is realized mainly for low concentrations of phytoplankton and in the blue region of the electromagnetic spectrum. The assumption of a uniform distribution of water-leaving radiance, as reported by Yang and Gordon (1997), leads to an error of up to 4% ($\lambda = 0.443$ and 0.555 μm) for observation angles $0° \leq \theta \leq 60°$ and $0° \leq \varphi \leq 180°$, and aerosol optical thicknesses $\tau_a(\lambda) \leq 0.2$ for a range of solar zenith angles $40° \leq \theta_0 \leq 60°$. Likewise, Zhao and Nakajima (1997) report errors in simultaneously retrieved water-leaving reflectance and aerosol optical thickness in the range of 10%. Better characterization of anisotropy of the water-leaving radiance field just above the ocean surface would certainly lead to smaller errors in the retrieved ocean biophysical products.

The sun's glitter (hereafter referred to as sun glint) pattern is perhaps one of the most studied optical features of the ocean (e.g., Hulburt 1934; Duntley 1954; Cox and Munk 1954a,b; Schooley 1954; Guinn et al. 1979; Preisendorfer and Mobley 1986). These studies have increased our knowledge not only of sun glint morphology, but also of the distribution of slopes and curvature at various wind speeds, parameters that are important in the reflection and refraction of acoustics and electromagnetic radiation. Although some satel-

lite-borne sensors, for example, Sea-viewing Wide Field-of-view Sensor (SeaWiFS), avoid sun glint—partly because no useful retrievals were envisaged during its design, and partly because of detector saturation problems—the sun-glint reflectance has been exploited in the retrieval of aerosol absorption (Kaufman et al. 2002) and precipitable water vapor in the near-infrared (Kleidman et al. 2000). The sun-glint observation and the detection of a small signal of the water-leaving radiances in directions away from the glitter, however, require a sensor with a stable response over a wide dynamical range.

In this study we discuss the anisotropy of the radiance field above the ocean surface from airborne measurements obtained over the Atlantic Ocean with NASA's CAR. To isolate the reflectance properties of the ocean surface in the absence of the atmosphere, we have developed a rigorous atmospheric correction algorithm for the CAR measurements based on the method of spherical harmonics (Lyapustin and Muldashev 1999, 2000). The algorithm models the water surface reflectance by the Cox–Munk model and assumes the water-leaving radiance to be Lambertian. The algorithm retrieves the wind speed from the sun-glint pattern and evaluates the equivalent albedo for the water-leaving radiance outside the glitter in the CAR spectral bands. Also contained in this study is an attempt to validate under the conditions we measured the widely used Cox–Munk model for predicting surface slope statistics as a function of wind speed.

The remainder of this paper is divided into four sections. Section 2, on measurements and methods, describes the main characteristics of the instrument, radiometric calibration, and BRDF measurement methodology. Section 3 discusses the method used to retrieve the BRDF. Section 4 presents our results of ocean BRDF and other derived parameters like the total albedo and the equivalent water-leaving albedo. Results of validation of the Cox–Munk model under the conditions we measured are discussed in this section. Section 5 concludes with a summary of the study.

2. Measurement methods

a. Description of the instrument

In the past we described in depth the Cloud Absorption Radiometer (King et al. 1986; Gatebe et al. 2003). In this study we only highlight some of the important characteristics of the instrument as summarized in Tables 1 and 2.

The CAR is an airborne multiwavelength scanning radiometer that measures scattered light in 14 spectral bands between 0.34 and 2.30 μm (Table 1). In the normal mode of operation, data are sampled simultaneously and continuously on nine individual detectors. Eight of the data channels for spectral bands from 0.34 to 1.27 μm are always registered during the operation, while the ninth data channel is registered for signal selected among six spectral channels (1.55–2.30 μm) on a filter wheel. The filter wheel can either cycle through all six spectral bands at a prescribed interval (usually changing filter every fifth scan line), or lock onto any one of the six spectral bands, mostly 1.656, 2.103, or 2.205 μm, and sample it continuously. The CAR scan mirror rotates 360° in a plane perpendicular to the direction of flight, and the data are collected through a 190° aperture that allows observations of the earth–atmosphere scene around the starboard horizon from local zenith to nadir. In this study we only report results of data analysis from channels between 0.472 and 1.219 μm. The UV bands were not analyzed because of a significant contribution of polarization, which is not taken into account in our algorithm. We also did not process measurements at 1.273 μm because the detected signal was systematically lower by 10%–20% than theoretically predicted, the discrepancy of which has not been identified. The filter wheel channels, on the other hand, were not consistently stable during measurements and therefore are excluded from our analysis.

Table 2 provides the signal-to-noise ratio (SNR) in our measurements of BRDF. We chose dark uniform scenes to compute the SNR. An average signal was determined from each scene, and then divided by the

TABLE 1. Cloud Absorption Radiometer specifications during CLAMS.

Parameters	Specifications
Platform	University of Washington CV-580 aircraft
Ground speed	80 m s^{-1} (nominal)
Total field of view	190°
Instantaneous field of view	17.5 mrad (1°)
Imaging modes	4 (zenith, BRDF, starboard, nadir)
Pixels per scan line	382
Scan rate	1.67 scan lines per second (100 rpm)
Spectral channels [μm; bandwidth: full width, half maximum (FWHM)]	14 (8 continuously sampled and last 6 in filter wheel: 0.340(0.009), 0.381(0.006), 0.472(0.021), 0.682(0.022), 0.870(0.022), 1.036(0.022), 1.219(0.022), 1.273(0.023), 1.556(0.032), 1.656(0.045), 1.737(0.040), 2.103(0.044), 2.205(0.042), 2.302(0.043)
Output channels	9 channels at 16 bits
Data rate	61.85 MB h^{-1}
Instrument mass	49 kg
Radiometric calibration	Laboratory integrating sphere measurements before and after research mission

TABLE 2. Signal-to-noise ratio for CAR measurements during CLAMS.

Date (2001)	Signal-to-noise ratio at λ (μm)					No. of points
	0.472	0.682	0.870	1.036	1.219	
10 Jul	733	133	86	21	19	1271
17 Jul	992	174	118	28	21	1806
23 Jul	775	45	32	8	7	1207
26 Jul	985	110	122	31	26	552
30 Jul	924	146	100	23	22	2121
31 Jul	1544	96	93	23	24	651
2 Aug	596	50	28	7	5	2511

standard deviation of the dark current, which was acquired for each data cycle when the detectors were all completely darkened. The radiometric performance of the CAR compares well with Moderate Resolution Imaging Spectroradiometer (MODIS), Multiangle Imaging Spectroradiometer (MISR), SeaWiFS, and Coastal Zone Color Scanner (CZCS). In Table 1 of Gordon (1997), the noise equivalent reflectance value at 0.490 μm for MODIS is 1.4×10^{-4}, SeaWiFS is 3.4×10^{-4}, and CAR values are between 2.0×10^{-5} and 6.0×10^{-5} at 0.472 μm. The noise equivalent reflectance value at 0.670 μm for MODIS is 4.0×10^{-5}, SeaWiFS is 2.3×10^{-4}, MISR is 1.7×10^{-4}, CZCS is 5.1×10^{-4}, and CAR ranges between 5.0×10^{-5} and 1.4×10^{-4} at 0.682 μm. This comparison clearly shows that the sensitivity of CAR, especially at 0.47, 0.68, and 0.87 μm, satisfies the accuracy requirements for low water-leaving radiances. On the other hand, relatively low SNR $Z \approx 20$ at 1.036 and 1.219 μm, although sufficient for analysis of the sun glint, may not be adequate for water-leaving reflectance retrievals.

b. Calibration of the CAR

Radiometric calibration was performed at Goddard Space Flight Center (GSFC) prior to and just after the CLAMS field experiment, at intervals of about 2 months. To determine a suitable calibration for a given flight during the experimental campaign, we assumed a linear change between pre- and postflight calibration and as a function of only the number of flights flown during CLAMS. In this case, there were a total of 12 flights flown, 2 during the instrument flight test, and 10 during the field experiment. We note that the calibration ratios postflight/preflight averaged about 0.98 for $0.472 \geq \lambda \geq 1.219$ μm. We used the spectral calibration of the CAR that defined the bandpass functions and central wavelengths conducted 1 yr before the CLAMS experiment, assuming that the CAR filter density functions remained stable based on our past experience (Gatebe et al. 2003).

c. Measurements of BRDF

To measure the BRDF of the surface–atmosphere system, the airplane flew in a circle about 3 km in diameter above the surface, taking roughly 2–3 min to complete an orbit (see Fig. 2). For the instrument to image from zenith to nadir, it had to be adjusted mechanically by a servo control system installed for the CLAMS experiment to allow the instrument to point at any angle between 0° and 180°, and to compensate for variations in airplane roll angle down to a fraction of a degree. In the past the airplane had to bank at an angle of 20° from the vertical with the instrument locked into an imaging mode that was set to allow CAR to image from zenith to nadir. The new method was found to produce better results in pointing and reduced tremendously the postprocessing analysis, particularly the geometrical rectification of the imagery. The CLAMS measurements over the ocean were generally obtained at an altitude of ~200 m above the surface and under clear-sky conditions. From an altitude of 200 m the pixel resolution is about 4 m at nadir and about 116 m at an 80° viewing angle, assuming a 1° instantaneous field of view (IFOV) of the CAR. Multiple circular orbits were acquired over a selected surface so that average BRDFs smooth out small-scale surface and atmospheric inhomogeneities. With this configuration, the CAR collects between 76 400 and 114 600 directional measurements of radiance per channel per complete orbit.

We believe using the CAR in this manner is the most mobile and efficient way of measuring a complete surface BRDF, but it is still necessary to make geometric corrections and account for atmospheric scattering effects both above and below the aircraft in order to isolate the reflectance properties of the underlying surface. Geometric correction is applied to remove image distortions through an algorithm developed for processing CAR level 1 data that allow pixels to be matched to their actual scan angle by use of airplane roll, pitch, and scan line pixel corresponding to the horizon (matched to a scan angle of 90°) that is easily identified on a scan line by the contrast between sky and surface, especially on a clear day. A plot of sky radiance as a function of azimuthal angle helps in identifying asymmetry due to errors in the geometrical correction. It should be noted here that the documented error of the differential global position system (Trimble TANS/ vector) is ±0.5°. In the next section we discuss atmospheric correction.

3. Retrieval of BRDF from measurements

Figure 2 shows a schematic representation of the instantaneous sea radiance received by the CAR aboard the aircraft, as it scans the surface from a height of 200 m as the airplane orbits a particular scene over the ocean. The total instantaneous sea radiance received by the CAR may be broken down into four components: (i) I_{sun}—radiance from the direct solar beam reflected by the ocean surface into the CAR's instantaneous field of view, (ii) I_{sky}—radiance from scattered photons in the atmosphere that are reflected by the ocean surface to the CAR, (iii) I_{path}—a part of the radiance along the

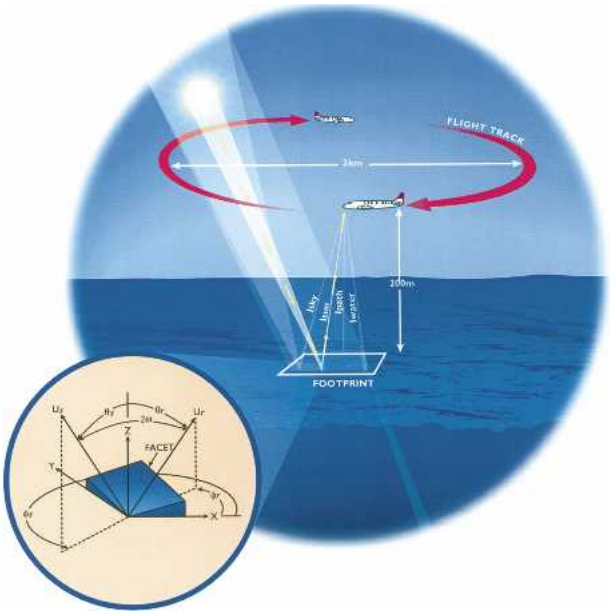

FIG. 2. Schematic representation of the BRDF measurements with CAR, scanning the surface from 200 m above the ocean surface as the aircraft makes a clockwise circular flight track. The radiance detected by the CAR may be broken down into four components: path radiance (I_{path}), sky radiance (I_{sky}), sun-glint radiance (I_{sun}), and radiance backscattered by the hydrosols to the CAR represented by I_{water}. The inset [modified after Cox and Munk (1954a)] shows the geometry of facet reflection with unit vectors U_s and U_r pointing toward the sun and the CAR, respectively, from the origin of a right-handed coordinate system located at the reflection point.

path from the footprint to the CAR scattered by air molecules and aerosols, and (iv) I_{water}—water-leaving radiance. Note that the footprint of a single pixel in an ocean image taken by the CAR, typically about 4 m on a side, assuming 200-m altitude and IFOV of 1°, is represented by the square box.

The actual three-dimensional situation for a single facet is shown in Fig. 2 (inset). The coordinate system used is such that the origin is the point of reflection with the x axis pointing upwind, the z axis pointing toward the zenith, and the y axis pointing crosswind such that a right-handed system is formed. The x–y plane is parallel to the mean sea level and horizontal at the point of reflection. The tilted facet passes through the origin. The facet slopes z_x and z_y in the x and y directions are given by the slope of the line formed by the intersection of the facet with the x–z and y–z planes, respectively. The two unit vectors U_s and U_r point from the origin to the source, and from the origin to the CAR, respectively. The normal to the facet at the origin, U_n, has been left out of the figure for clarity. Each unit vector is specified by its zenith angle θ and its azimuth angle φ. In general, the three vectors may point in arbitrary directions and are connected by the law of specular reflection in the form: $U_s + U_r = 2\cos\omega U_n$, where ω is the angle of incidence and angle of reflection.

In this study we developed a new algorithm for atmospheric correction of CAR measurements to retrieve surface BRDF from the above four components. The method of spherical harmonics with Cox–Munk (1954a,b) wave-slope distribution is used here to solve the atmosphere–ocean radiation transport problem. The basic method is described in several studies (e.g., Lyapustin and Muldashev 1999, 2000). The numerical implementation of this method is named here as SHARM. We provide below an overview of the method in the context of the new algorithm.

a. Algorithm description

We use the lower boundary condition of the equation of radiative transfer for ocean–atmosphere system to find the reflected radiance $I(H;\mu_r,\varphi_r)$ in the directions (μ_r, φ_r) for the specified BRDF $R(\mu', \mu_r, \varphi_r - \varphi')$ written in the form

$$I(\mu_r, \varphi_r) = F_0 e^{-\tau/\mu_0}\mu_0 R(\mu_0, \mu_r, \varphi_r - \varphi_0) + \frac{1}{\pi}\int_0^{2\pi} d\varphi' \int_0^1 I(\mu', \mu_r, \varphi)\mu' R(\mu', \mu_r, \varphi_r - \varphi')d\mu'. \quad (1)$$

Here, F_0 is the extraterrestrial solar spectral irradiance; τ_λ is the atmospheric optical thickness; and $\mu_r = \cos\varphi_r$, $\mu_0 = \cos\theta_0$, and φ denote azimuthal directions as described above. In our notation, $\mu < 0$ for the upward directions, and $\mu > 0$ otherwise; $R = R_{CM} + R_W$ is the total BRDF of the ocean. It consists of reflectance of the water surface R_{CM} and of the bulk of water and foam R_W. In this study we used the Cox–Munk (1954a,b) model for simulating reflectance of the sun glint and the Nakajima and Tanaka (1983) model, hereafter referred to as modified Cox–Munk model, for the reflectance of the wind-ruffled ocean surface outside the glitter in the form

$$R_{CM}(\mu',\mu_r, \varphi_r - \varphi) = \frac{\pi}{\mu'}\frac{1}{4\mu_r\mu_n} R_{Fr}(\omega)P(\mu_n)S(\mu',\mu_r), \quad (2)$$

where $R_{Fr}(\omega)$ is the Fresnel reflectance in terms of reflection angle (cf. Fig. 2, inset); $P(\mu_n)$ is the probability density function of slope distribution, with n referring to the orientation of the normal to the wave facet with respect to the z axis; and $S(\mu', \mu_r)$ is the bidirectional shadowing factor defining the conditional probability of occurrence of an event that the wave facet with surface normal n contributes to the reflection of light. The functions $P(\mu_n)$ and $S(\mu', \mu_r)$ depend on the mean square slope, which linearly grows with the wind speed u as $\sigma^2 = 0.00534u$. Note that u (meters per second) is measured 10 m above the water surface. The Fresnel reflection coefficients were calculated based on refractive indices of water taken from Hale and Querry (1973).

We write the solution of the radiative transfer equation at the flight level z in the following form, separating the direct surface reflected term:

$$I(z; \mu_r, \varphi_r) = F_0\mu_0 R(\mu_0, \mu_r, \Delta\varphi_0) e^{-\frac{\tau_0}{\mu_0}} e^{-\frac{\tau_0-\tau(z)}{|\mu_r|}} + I_{\text{sky}}(z; R) + I_{\text{path}}(z), \quad (3)$$

where $I_{\text{sky}}(z; R)$ is the diffuse (atmospherically scattered) radiance at altitude z that has undergone interactions with the ocean. We have assumed that the water-leaving reflectance does not depend on the angle of incidence. This approximation is only used to calculate the diffuse upwelling radiance $I_{\text{sky}}(z; R)$ while the direct reflected component (and BRDF) is found explicitly from measurements, retaining the directional features of the water-leaving radiance. This approach mitigates possible error in the BRDF retrieval while keeping high efficacy of the algorithm. On the other hand, it can introduce a small offset that is variable with θ_0 to the diffuse water-leaving BRDF retrieved from the direct term. To perform atmospheric correction of CAR BRDF measurements, (3) is rewritten in the form

$$R(\mu_0, \mu_r, \Delta\varphi_0) = [I_{\text{CAR}}(\mu_r, \Delta\varphi_0) - I_{\text{path}}(z) - I^{(k)}_{\text{sky}}(z)] \Big/ \left[F_0\mu_0 e^{-\frac{\tau_0}{\mu_0}} e^{-\frac{\tau_0-\tau(z)}{|\mu_r|}}\right]. \quad (4)$$

The iterative procedure of BRDF retrieval may be summarized as follows:

1) On the first iteration $k = 1$ initialize $u^{(k-1)} = 1\text{m s}^{-1}$, $R_W^{(k-1)} = A_w^{(k-1)} = 0$, $R = R_{\text{CM}}^{(k-1)}$.
2) Compute $I^{(k)}_{\text{sky}}(z; R)$.
3) Compute the full BRDF for all view angles of the CAR using

$$R^{(k+1)} = [I_{\text{CAR}} - I_{\text{path}}(z) - I^{(k)}_{\text{sky}}(z)] \Big/ \left[F_0\mu_0 e^{-\frac{\tau_0}{\mu_0}} e^{-\frac{\tau_0-\tau(z)}{|\mu_r|}}\right].$$

4) In the glint region, defined as $R^{(k+1)}(\mu_0, \mu_r, \Delta\varphi) > \max[R_W^{(k)}, 0.02]$, find the best-fit wind speed $u^{(k+1)}$ for the difference $R^{(k+1)} - R_W^{(k)}$, and update $R_{\text{CM}}^{(k+1)}$.
5) Update R_W and average water-leaving albedo over the dark ocean. For angles $(\theta_r^j, \varphi_r^j)$ where $R_{\text{CM}}^{(k+1)} < 0.001$, compute $R_W^{(k+1)} = R^{(k+1)} - R_{\text{CM}}^{(k+1)}$. Next, find the average water-leaving albedo $A_W^{(k+1)} = N^{-1}\Sigma_j R_{W,j}^{(k+1)}$, which substitutes R_{W} for the glint region in the direct reflected radiance and is used to find the diffuse reflected radiance. In this step, we eliminated high zenith angles ($\theta_r > 60°$), where the retrieved BRDF exhibits strongly non-Lambertian behavior and becomes more sensitive to the uncertainties in the atmospheric properties (aerosol, water vapor, and atmospheric inhomogeneity).
6) Repeat iteration from step 2 until the wind speed and the water-leaving albedo stabilize.

This procedure is repeated twice. The first stage serves to retrieve a best estimate of the wind speed. The processing is performed independently for different spectral bands, so the magnitude of the dispersion between independent retrievals serves as an additional quality indicator. After this iteration, the average wind speed is fixed and used in all spectral bands to retrieve the water-leaving BRDF and albedo.

Figure 3 illustrates this iterative procedure for performing atmospheric correction and deriving surface wind speed from multispectral CAR measurements. While processing experimental data we found that in the blue band the convergence strongly depended on an initial guess of $R_W^{(k=0)}$. Convergence can be weak with the solution fluctuating around the true value. To remedy this situation, we used the relaxation technique based on the value from the previous iteration:

$$A_W^{(k+1)} = A_W^k + \alpha\left[\frac{1}{N}\sum_{j=1,N} R_{W,j}^{(k+1)} - A_W^k\right], \quad (5)$$

where α is a relaxation parameter. We found that using $\alpha = 0.7$ ensures stable convergence in two–four iterations for all of the processed cases both in clear and hazy conditions.

Although the CAR channels were carefully selected in the atmospheric windows, there is still an appreciable amount of absorption by water vapor and atmospheric oxygen. We calculated the line-by-line gaseous absorption based on the latest high-resolution transmission-2000 (HITRAN-2000) molecular absorption database (Rothman et al. 2003) for the *U.S. Standard Atmosphere, 1976* profile using the Voigt line shape. A step of 0.01 cm^{-1} in the shortwave region of interest guarantees resolution of lines of major atmospheric gases whose half-width typically exceeds 0.04–0.05 cm^{-1}. As an example, Fig. 4 shows the calculated vertical atmospheric transmission of water vapor at $\lambda = 1.219$ μm averaged over 1 cm^{-1} for total column water vapor $q = 3.15$ g cm^{-2} (2.16 g cm^{-2} above the aircraft) on 10 July 2001.

Since gaseous absorption decreases the magnitude of the glint reflectance, it affects the wind speed retrievals in our algorithm. The difference in gaseous absorption among CAR channels leads to an additional dispersion in the retrieved velocities of the wind. After explicitly accounting for gaseous absorption, we found that the dispersion of the retrieved wind speed among different CAR channels decreased by about 0.5 m s^{-1}.

b. Auxiliary data for atmospheric correction

The aerosol and water vapor distribution for each of the two layers of the atmosphere (with interfaces at $z = 0.0$, ~0.2, and 100.0 km) were determined from the

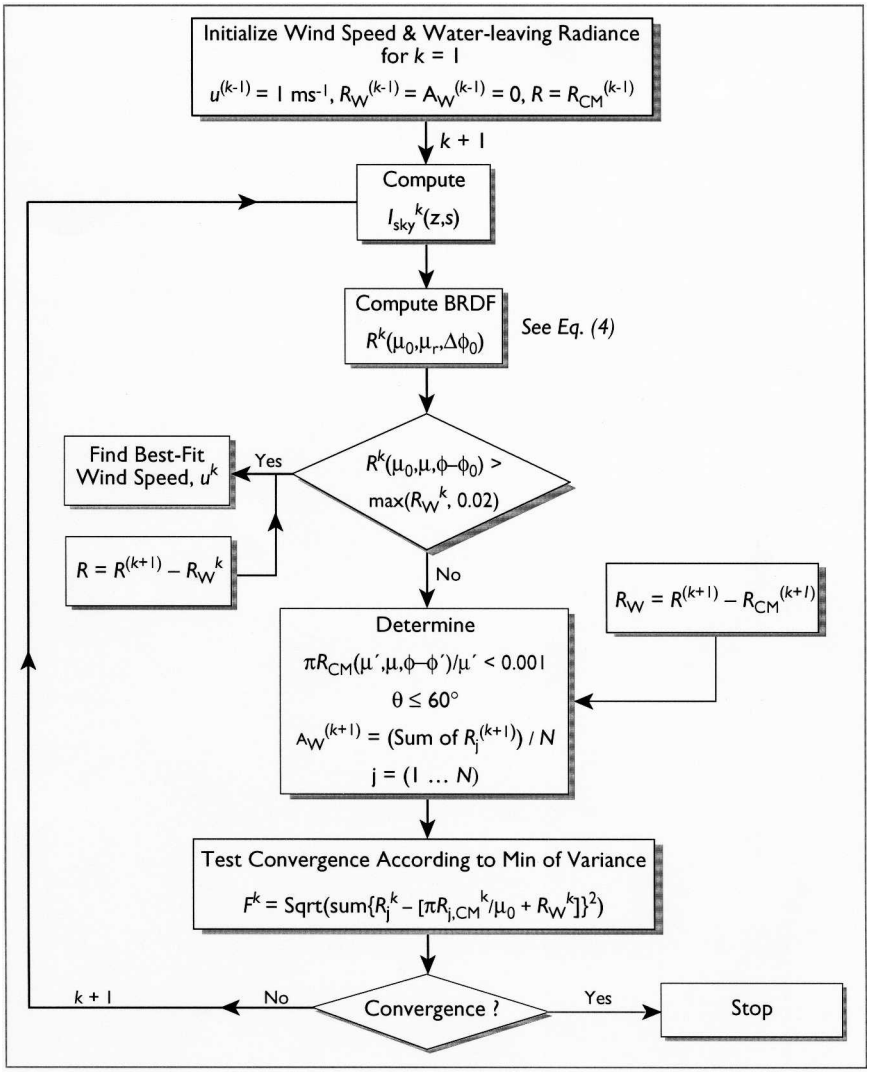

FIG. 3. Flow diagram for the atmospheric correction of CAR BRDF measurements.

14-channel Ames Airborne Tracking Sunphotometer (AATS-14; Redemann et al. 2005). AATS-14 obtained measurements of aerosol optical depth and water vapor at 14 discrete channels in the UV, visible (VIS), and near-infrared (NIR) regions of the electromagnetic spectrum at the same locations and time as the CAR BRDF measurements, thereby characterizing the atmosphere above the airplane. To estimate the total aerosol optical thickness and water vapor, we used the AATS measurements at the lowest flight altitude (~50 m) closest in time to the BRDF observations. The concurrent sun-photometer measurements of the Aerosol Robotic Network (AERONET) at the Chesapeake Lighthouse were used to constrain and adjust our estimates of the total column aerosol optical thickness and water vapor content. To model aerosol optical properties, we used the AERONET size distribution and index of refraction (Dubovik et al. 2002). Further, we assumed that the aerosol phase function and single scattering albedo were the same above and below the airplane.

Thus, we established a procedure for processing CAR data involving monochromatic radiative transfer with the Cox–Munk surface reflectance model and accounting for gaseous absorption and the water-leaving radiance in the CAR channels.

c. *Illustration of atmospheric correction*

In this section we apply the algorithm on measurements taken on 17 July near Chesapeake Light as a way to illustrate its performance. On this day the AATS aerosol optical depth is much higher than on any other day during the field experiment (see Fig. 5). For example, $\tau_a(0.472\ \mu\text{m}) = 0.423$ on 17 July and was less than 0.2 on all the other flight days. Other ancillary information like the water vapor column needed for atmospheric correction is also available. This makes it a

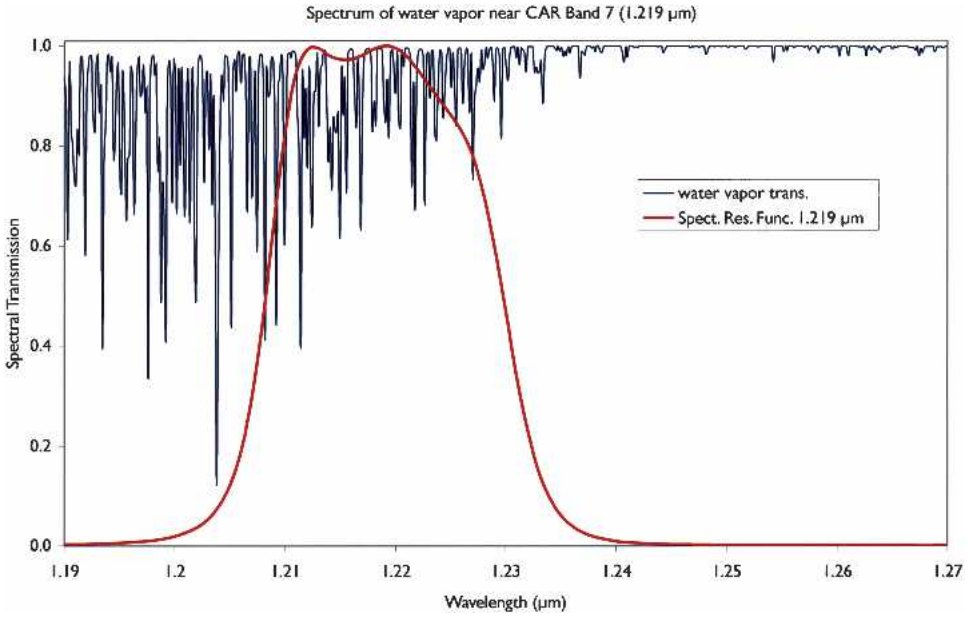

FIG. 4. Calculated vertical atmospheric transmission of water vapor averaged over 1 cm^{-1} for the CAR band at a wavelength of 1.219 μm for total column water vapor $q = 3.15$ g cm^{-2} (2.16 g cm^{-2} above the aircraft) on 10 Jul 2001. The spectral response function at the same wavelength is superimposed.

good case to test the robustness of this atmospheric correction algorithm.

Figure 6a shows a transect of reflectance through the principal plane (the vertical plane containing the sun) for five discrete wavelengths between 0.472 and 1.219 μm as seen from the CV-580 aircraft. The reflectance curves are given as a function of the angle of observation $-80° \geq \theta \geq 80°$. With this notation, the negative angles represent backscattering directions, and the positive angles forward-scattering directions. The surface wind was 6.14 m s^{-1} (measured at 43.3 m), and the average solar zenith angle $\theta_0 = 16.23°$. As expected,

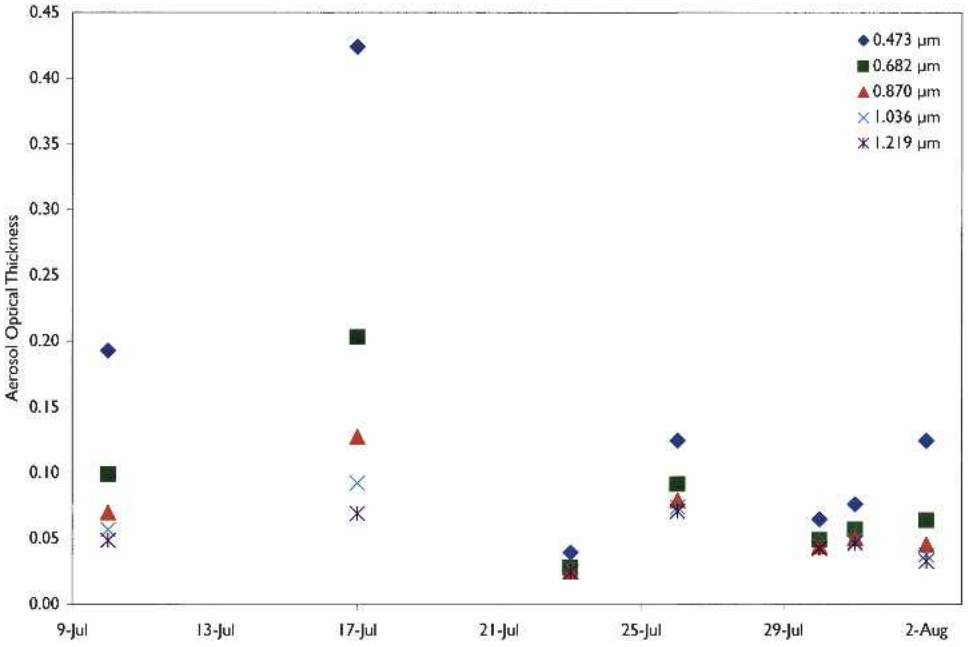

FIG. 5. Variation of $\tau_a^{\text{aircraft}}(\lambda)$ as measured by AATS during the CLAMS field experiment campaign at the time of BRDF measurements.

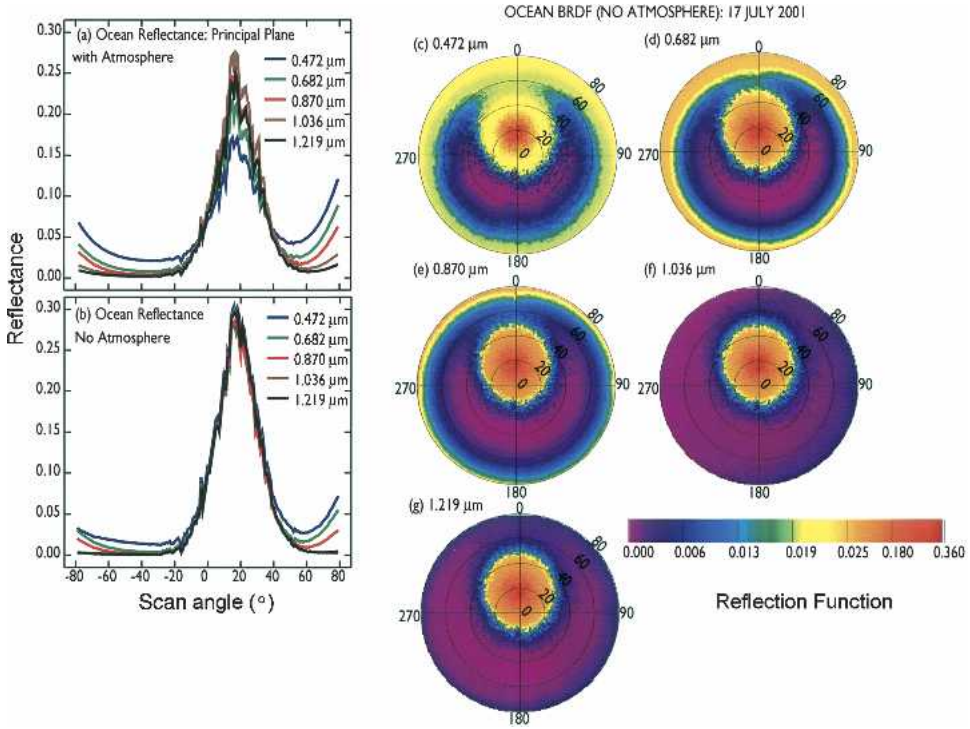

FIG. 6. Illustration of atmospheric correction. (a), (b) The angular distribution of bidirectional reflectance in the principal plane for measurements taken on 17 Jul 2001 at 36.96°N, 75.72°W in the vicinity of Chesapeake Light (36.91°N, 75.71°W) before and after atmospheric correction. (c)–(g) The full atmospherically corrected BRDF for five CAR spectral channels in the visible and near-infrared. The broad reflectance peak represent the sun glint for an average solar zenith angle $\theta_0 = 16.23°$.

the maximum reflectance values at these solar wavelengths are near the angle for specular reflection from the ocean spread into a range of observation angles. As we move away from this broad solar image peak, the reflected radiance starts to fall off rapidly before starting to increase more rapidly, especially in the forward direction, due to multiple scattering effects of the atmosphere. Since Rayleigh scattering decreases with λ, we see relatively more scattering in the blue ($\lambda = 0.472$ μm) as we move toward the horizon. Using the new algorithm, we removed the effects of Rayleigh scattering, aerosol attenuation, and ozone and water vapor absorption. Figure 6b shows the resulting curves for reflected radiance just above the ocean. To obtain these results we specified the aerosol optical depth above the airplane [details of aerosol measurements during CLAMS are found in Redemann et al. (2005)]. As explained in section 3b, the total aerosol optical thickness and water vapor were estimated from the AATS measurements at the lowest flight altitude (~50 m) closest in time to the BRDF measurements. The aerosol-scattering function and single scattering albedo, ω_λ are determined by Mie theory for a lognormal size distribution of aerosol derived from AERONET measurements at Chesapeake Lighthouse on 17 July.

Thus, using the new algorithm, we retrieved atmospherically corrected BRDF, R_λ, just above the ocean surface that retains specific features of the measured reflectance in the direction of the measurements. We now discuss results of all the cloud-free BRDF measurements acquired during CLAMS.

4. Results and discussions

Table 3 shows information on location, date, time, and general conditions of our measurements for seven cloud-free BRDF experiments. The average wind speeds range from 1 to 11 m s^{-1}. The sun was generally high, and the range of solar zenith angles was relatively narrow (15°–33°). One exception is the case of 2 August, when solar zenith angle was on average 44°. The measurements (10 July, 17 July, 30 July, and 2 August) were obtained in the vicinity of the NOAA station CHLV2 (Chesapeake Light; 36.91°N, 75.71°W) where ocean water depth is 11 m. The station is located ~20 km off Virginia Beach, Virginia, on the eastern coast of the United States. The other experiments were conducted around three different NOAA buoy stations: 44009 (38.46°N, 74.70°W; water depth 28 m) on 23 July, 44014 (36.58°N, 74.84°W; water depth 47 m) on 26 July, and 44004 (38.50°N, 70.47°W; water depth 3160 m) on

TABLE 3. CAR BRDF measurements parameters for CLAMS.

Date (2001)	Time (UTC)	Location	Solar (θ_0, φ)(°)	Measured u (m s^{-1}), altitude (retrieved u;* 10 m)
10 Jul	1804–1819	36.96°N, 75.70°W	19–22, 223–231	1.58; 43.3 m (2.1–2.4)
17 Jul	1646–1705	36.96°N, 75.72°W	15–16, 160–177	6.14; 43.4 m (4.1–4.6)
23 Jul	1501–1518	37.82°N, 74.36°W	29–33, 115–121	1.08; 5 m (1.1–1.2)
26 Jul	1748–1806	36.48°N, 74.51°W	19–22, 211–223	9.10; 5 m (9.6–11.5)
30 Jul	1905–1919	37.09°N, 75.61°W	31–35, 241–246	10.56; 43.3 m (9.5–13.1)
31 Jul	1652–1706	38.55°N, 70.64°W	20–21, 182–192	8.41; 4 m (10.0–11.3)
2 Aug	2000–2019	37.08°N, 75.68°W	42–46, 254–259	2.88; 43.3 m (2.6–2.7)

* Computed using the Cox–Munk model as described in section 3a.

31 July. The actual locations of BRDF measurements relative to the buoy stations are shown in Fig. 1. The background image in this figure is the MODIS true color image from Earth Observing System (EOS) *Terra* acquired on 13 April 2003. A suitable image free from clouds and/or sun glint for the period of measurements was not available.

Since the CAR BRDF measurements were obtained at an altitude of ~200 m above sea level with the instrument in the nose cone of University of Washington CV-580 (dimensions: length = 25.0 m, height = 9.0 m, wing span = 32.2 m), the aircraft shadow was observed to contaminate the data. The shadow appears in the data as an anomalously dark zone in the antisolar plane ($\varphi = 180°$) and in directions corresponding to $\theta = \theta_0$. The shadow is observed in all bands, but is most distinct at 0.472 μm. We have compared pixel-level data in the shadow and outside the shadow. The maximum reflectance differences range from 0.004 to 0.009 at 0.472 μm. The differences are less than 0.004 at 0.682 and 0.870 μm. We could have minimized the shadowing effect had the measurements been obtained from a much higher altitude, say $H > 600$ m. This would, on the other hand, have meant decreasing the spatial resolution of our measurements and increasing the uncertainty of atmospheric correction that we wanted to minimize. A similar effect of self-shadowing is reported by Morel et al. (1995) for measurements made aboard a ship with a submersible camera system (Voss 1989).

Because of the high resolution of our measurements, both angular (1°) and spatial (better than 4 m at nadir), coupled with high SNR (cf. Table 2) and small quantization interval (16 bits), we are able to see the radiance field above the ocean in unprecedented detail. In the following subsections we show the full BRDF with several patterns of sun glint and with notable anisotropy of the water-leaving radiance corresponding to various illumination and environmental conditions of our measurements. While discussing water-leaving BRDF, we focus on three spectral channels ($\lambda = 0.472$, 0.682 and 0.870 μm) that are used widely in remote sensing of ocean color and aerosol over the ocean. These wavelengths allow us to examine ocean optical properties for spectral regions with high transmission in the ocean (e.g., $\lambda = 0.472$ μm) and greater absorption of light in the ocean (e.g., $\lambda = 0.870$ μm).

a. Full ocean BRDF

In this study, we separately processed data using two models: modified Cox–Munk by Nakajima and Tanaka (1983), and Cox–Munk with and without the Gram–Charlier expansion. The Cox–Munk model is incorporated in the radiative transfer code SHARM only in the direct reflected radiance, while the diffuse radiance is computed with the modified Cox–Munk model. We generally discuss results of the Cox–Munk model with the Gram–Charlier expansion and later in section 4e(2) compare measurements to simulations using each of the models.

Figure 7 shows BRDFs, $R_{0.472}(\theta,\varphi)$, just above the ocean surface for $0° \geq \theta \geq 80°$ and $0° \geq \varphi \geq 360°$; where φ represents the azimuth difference between CAR viewing azimuth and the sun azimuth ($\varphi = \varphi_{CAR} - \varphi_0$) for the seven cloud-free cases. Figures 7h and 7i show transects of reflectance through the principal and perpendicular planes for the seven cases shown in the polar plots. Each case represents a different combination of solar zenith angle and wind condition as shown in Fig. 7h. It is interesting to note that for all cases except for Fig. 7f, which represents the BRDF of deep ocean belonging to oceanic Case I waters (open waters), the rest of these observations that appear to be Case II waters were obtained close to the coastline. According to Morel (1988), the optical properties of Case I waters are mainly influenced by the concentration of phytoplankton and their derivative products, whereas the properties of Case II waters are influenced by suspended sediments or dissolved yellow substance. Morel further observes that, "in absence of terrigenous influx (along arid coasts) and of resuspended sediment from the shelf, coastal waters can also, and often do, belong to Case I." Although it is feasible that the waters we obtained BRDF measurements over may have been under the influence of deep ocean waters, we see a marked contrast in BRDF pattern from the locations close to the coastline and open ocean.

We chose to separate our discussion of the sun glint pattern from the water-leaving radiance because of the large difference in magnitude of the signals from the

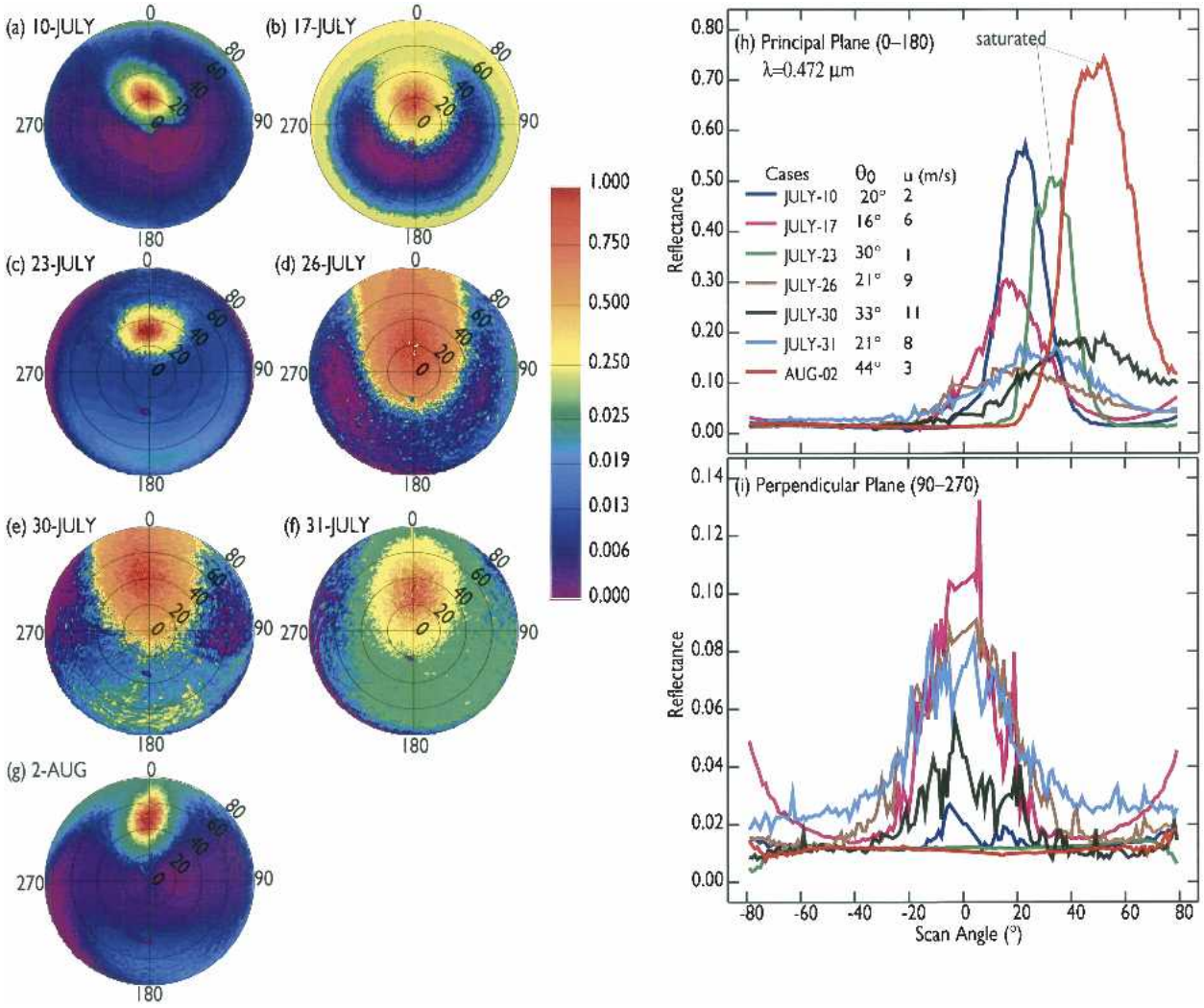

FIG. 7. Spectral BRDF at 0.472 μm for seven cloud-free cases obtained by CAR between 10 Jul and 2 Aug 2001 during CLAMS. The transects through and perpendicular to the plane of the sun are also given. The effect of different illumination and wind conditions on the intensity, size, orientation, and location of sun glint is clearly seen.

sun glint and water-leaving radiance that makes it hard to compare them on the same linear scale. Furthermore, the two have different histories; the sun glint seems to be well studied, whereas the water-leaving radiance is much less studied, and for a long time was regarded as dark ocean.

b. Sun-glint BRDF

Before we begin our discussion on sun glint it is important to point out that at resolutions in the order of meters, capillary waves are indistinguishable and the sun glint registered by CAR would be an average of numerous sun glints over a pixel. Since, as pointed out earlier, the pixel resolution is about 4 m at nadir, and about 116 m at an 80° viewing angle, assuming an altitude of 200 m and a 1° instantaneous field of view of the CAR. This implies smoother sun-glint reflectance for CAR pixels at grazing angles. At this resolution gravity waves would play a modulating role (cf. Walker 1994, p. 413).

In each case we studied, we observed a pronounced sun-glint pattern. The sun-glint pattern consists of numerous instantaneous sun glints produced by direct reflection of the sun into the directions near the angle of specular reflection from the ocean. The sun-glint patterns have a shape that is either elliptical (Fig. 7a) or roughly circular (Fig. 7b), with a glint peak ranging from 0.147 (26 July) to 0.631 (10 July), excluding the two cases (23 July and 2 August) when the detector saturated. The peak reflectance does not seem to occur always in the principal plane. For example, on 10 July the peak reflectance in the principal plane ($\varphi = 0°$) is 0.572 at $\theta = 22°$, whereas the actual peak (0.631) occurs

at $\theta = 22°$ and $\varphi = 353°$. Table 4 shows the peak reflectance and its geometrical location, not only at $\lambda = 0.472$ μm, but also at other CAR spectral channels considered in this study (0.682, 0.870, 1.036, and 1.219 μm). We note that maximum reflectance is not always in the principal plane (cf. Cox and Munk 1955, p. 66) and that the angle of specular reflection is not always coincident in all channels even though the observations were obtained simultaneously with the same system as described in section 2a. It is not clear why the angle of specular reflection is not coincident across channels.

It is apparent from Fig. 7 that the location and size of the sun-glint patterns formed by the sun depend on the location of the solar zenith angle and the roughness of the water surface. It appears the sun-glint pattern is much wider on days when the wind is strong and the solar zenith angle is relatively large (e.g., 26 July, 30 July, and 31 July). The peak reflectance as seen in Fig. 7h is dependent upon wind speed and solar zenith angle. Small sun angle ($\theta_0 < 20°$) seems to favor a circular sun-glint pattern and relatively smaller peak, while a large sun angle favors an elliptical shape elongated toward the horizon and relatively broader peak. The wind direction clearly influences the orientation of the sun glint pattern.

Let us now turn to the diffuse radiative regime just above the water surface and outside the sun-glint pattern.

c. Water-leaving BRDF

At present, most of our knowledge of the angular distribution of the water-leaving radiance comes from theoretical simulations (e.g., Morel et al. 2002; Loisel and Morel 2002; Yan et al. 2002). These studies predict that under all conditions, water-leaving BRDF depends on θ_0. It decreases with increasing θ_0 because less light penetrates through the air–water surface into the bulk of the water. Furthermore, the studies report that water-leaving BRDF is controlled by single scattering when there is an abundance of absorbing yellow substances and anisotropy is maximal. The anisotropy in Case II waters decreases when dominated by sediment, where multiple scattering prevails.

There are also some measurements of the water-leaving radiance from ships and automatic platforms as part of validation programs of ocean color algorithms (e.g., Hooker and McClain 2000; Zibordi et al. 2002). The standard measurements are only conducted for several angles ($\varphi - \varphi_0 = 90°$, $\theta = 30°$, 40°, 45°) and fixed heights/depths as prescribed by the SeaWiFS Ocean Optics Protocol (Mueller and Austin 1995) and do not represent the full angular distribution. The

TABLE 4. Peak sun glint reflectance and peak reflectance in the principal plane, where R^P is peak reflectance in the principal plane.

Date (2001)		Reflectance at λ (μm)				
		0.472	0.682	0.870	1.036	1.219
10 Jul	Peak R	0.631	0.611	0.569	0.649	0.632
	(θ, φ)	(21, 353)	(20, 5)	(23, 354)	(20, 5)	(20, 5)
	Peak R^P	0.572	0.524	0.502	0.561	0.546
	(θ, φ)	(22, 0)	(22, 0)	(22, 0)	(22, 0)	(22, 0)
17 Jul	Peak R	0.355	0.337	0.338	0.355	0.354
	(θ, φ)	(16, 354)	(18, 3)	(15, 355)	(16, 354)	(15, 355)
	Peak R^P	0.305	0.284	0.285	0.300	0.297
	(θ, φ)	(15, 0)	(15, 0)	(15, 0)	(15, 0)	(17, 0)
23 Jul*	Peak R	0.532	1.092	0.854	1.836	1.869
	(θ, φ)	(32, 347)	(32, 355)	(32, 356)	(32, 355)	(32, 355)
	Peak R^P	0.506	0.964	0.813	1.438	1.455
	(θ, φ)	(32, 0)	(32, 0)	(32, 0)	(32, 0)	(32, 0)
26 Jul	Peak R	0.147	0.125	0.123	0.134	0.136
	(θ, φ)	(18, 8)	(18, 8)	(18, 8)	(24, 351)	(24, 351)
	Peak R^P	0.129	0.112	0.110	0.119	0.122
	(θ, φ)	(19, 0)	(10, 0)	(10, 0)	(18, 0)	(18, 0)
30 Jul	Peak R	0.245	0.238	0.226	0.235	0.246
	(θ, φ)	(37, 345)	(51, 348)	(54, 351)	(37, 345)	(37, 345)
	Peak R^P	0.193	0.185	0.176	0.175	0.184
	(θ, φ)	(51, 0)	(51, 0)	(51, 0)	(43, 0)	(43, 0)
31 Jul	Peak R	0.198	0.156	0.149	0.167	0.164
	(θ, φ)	(22, 9)	(22, 9)	(22, 8)	(22, 8)	(33, 2)
	Peak R^P	0.173	0.139	0.135	0.148	0.148
	(θ, φ)	(20, 0)	(20, 0)	(20, 0)	(20, 0)	(20, 0)
2 Aug*	Peak R	0.773	1.253	1.046	1.331	1.402
	(θ, φ)	(44, 358)	(50, 357)	(47, 2)	(45, 2)	(45, 2)
	Peak R^P	0.744	1.028	0.971	1.050	1.118
	(θ, φ)	(51, 0)	(47, 0)	(47, 0)	(47, 0)	(47, 0)

* $\lambda = 0.472$, 0.682, and 0.870 μm saturated.

known problems of underwater measurements are self-shading and high absorption, especially in the red spectrum, which make extrapolation difficult (Hooker et al. 2002). The above-water measurements need to eliminate the reflected sky radiance that may be much larger than the water-leaving radiance. Fougnie et al. (1999) resolved the problem by making above-water polarimetric measurements at the Brewster angle and a relative azimuth angle of 135°. This geometry allowed them to cut off the "noise" reflectance from the ocean surface down to about 10^{-4} reflectance units, 2%–10% of the signal of interest.

Because the magnitude of the water-leaving reflectance is at least an order of magnitude lower than in the sun-glint pattern (see also a transect through a plane perpendicular to the principal plane; Fig. 7i), we have eliminated the glint pattern using a threshold defined by $R_{CM} < 0.001$ [see also Eq. (2)]. That is, if computed reflectance for particular measurement geometry is less than 0.001, then the retrieved BRDF for the corresponding geometry is assumed to be in the diffuse radiative regime. This procedure allows us to eliminate the glint and provides a better view of the small variation in the water-leaving reflectance. This criterion seems to work well for the range of wind speeds encountered (1–11 m s^{-1}) without the biases of the high reflectivity of whitecaps assumed significant at high wind speed (>15 m s^{-1}; Nakajima and Tanaka 1983).

Figure 8 shows transects through the principal and perpendicular planes for all seven cases (now without the sun-glint pattern) for $\lambda = 0.472$, 0.682, and 0.870 μm. The data points (spaced 1° apart) in the principal plane are plotted as dots, while those in the perpendicular plane are plotted as triangles for each channel. The data points are joined with a thin line, continuous for points in the principal plane and dotted for points in the perpendicular plane. This differentiation makes it easy to follow each case separately. Note the range of view angles for 30 July (Fig. 8g) ranges from −80° to −40°. The different vertical scales help bring out the shape of the BRDF, bow shape, especially at $\lambda = 0.682$ and 0.870 μm. Note also the appearance of shadow contamination in the principal plane, especially on 10 and 23 July and 2 August (Figs. 8a, 8c, and 8f). From Fig. 8c it is apparent that the glint threshold did not work well in the principal plane. This is probably caused by a weakness in the Cox–Munk model at low wind speeds where it tends to underestimate reflectance as discussed in a later section, or uncertainty in atmospheric correction process, or both.

Figure 8 is interesting in several important ways. The BRDF $R_{0.472}(\theta) < 0.02$ for all cases except 31 July (Fig. 8e), which belongs to oceanic Case I waters; for $\theta \leq 60°$. The BRDF $R_{0.870}$ can be represented as $0.001 < R_{0.870} < 0.005$ for $\theta \geq 70°$ regardless of whether it is in the principal or perpendicular plane. It has been customary to assume that $R_{0.870} = 0.000$ in order to make an assessment of aerosol contribution over the ocean (e.g., Gordon and Wang 1994; Zhao and Nakajima 1997). The water-leaving reflectance has a typical shape that depicts near-constant values at $\theta \leq 40°$, a gradual increase for $40° < \theta \leq 60°$, and then a relatively steep increase at $\theta > 60°$. An exception to this rule is 30 July with a measured wind speed of 11 m s^{-1} and where $R_{0.870}$ show little variation for $\theta > 60°$.

In Fig. 9 we have selected the cases with low wind speeds: 10 July, 23 July, and 2 August for three channels for intercomparison of the full water-leaving BRDFs and of transects through the perpendicular plane. We see a clear anisotropy of the radiance field on all days, especially at 0.472 μm. The smooth angular variation makes it easy to fit the data with simple analytical functions. At 0.682 and 0.870 μm, R_λ is weakly dependent on the relative azimuth angle φ, and therefore the Lambertian approximation to the radiance field would be valid for these low wind speeds.

These results are in excellent overall agreement with measurements of Fougnie et al. (1999) and of theoretical simulations (e.g., Morel et al. 2002; Loisel and Morel 2001; Yan et al. 2002). For the case of 23 July, the BRDF in the blue band decreases at $\theta > 60°$, and the cause is not clear to us since the aerosol optical thickness was the lowest overall for this day. For view angles less than 60° the water-leaving radiance is practically isotropic at all wavelengths, which to some extent justifies the use of the Lambertian assumption in our algorithm, and more broadly, in the SeaWiFS and MODIS ocean color algorithms. The water-leaving reflectance does not show a strong dependence on solar zenith angle as suggested by theoretical simulations (e.g., Morel et al. 2002; Loisel and Morel 2001).

The derived water-leaving reflectance in all bands is very stable and consistently reproduced despite the low water-leaving signal and rather considerable variability of atmospheric conditions. There are a few cases of small negative reflectance in the NIR band. This may be due to experimental errors, failure of the radiative transfer model, uncertainty of aerosol correction, and/or calibration errors.

d. Ocean albedo and average water-leaving radiance

In this section we discuss the spectral albedo derived from our measurements (Fig. 10). Theoretically, we define albedo as the ratio of upward-propagating to downward-propagating irradiance just above the water surface. The upward-propagating irradiance includes radiance reflected from the surface into all viewing directions and solid angles and the upward irradiance transmitted through the water surface from the ambient light field within the water. The albedo therefore depends on the optical properties of the ocean surface and the body of water below, as well as the skylighting conditions. In this study we derive the spectral albedo by integrating the reflection over the solid angle in all di-

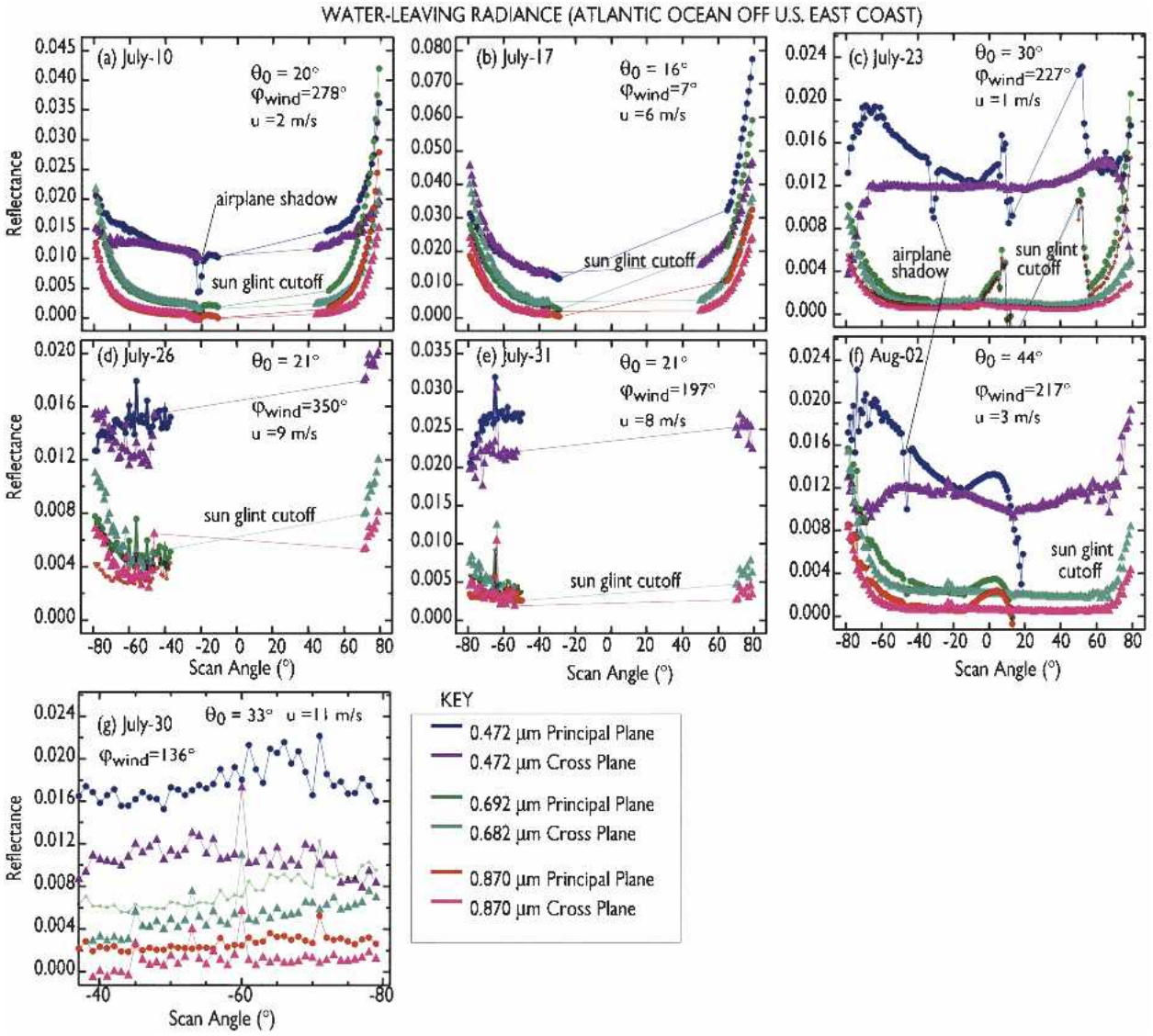

FIG. 8. Water-leaving BRDF in the principal and perpendicular plane of the sun at three CAR channels (0.472, 0.682, and 0.870 μm) for seven cloud-free cases with various conditions. On average, even though the illumination conditions are different, water-leaving BRDFs do not seem to vary much from case to case. Note that 31 Jul measurements were obtained in deep ocean unlike the other cases where measurements were obtained in the proximity of the coastline. The sun glint has been cut off so as to be able to amplify the low-varying BRDFs.

rections. On the other hand, the average water-leaving albedo is derived by integrating the isotropic reflection function outside the sun-glint pattern for all reflectances less than 0.02.

The solid lines of Fig. 10 show the spectral albedo as a function of time, computed from an integration of the atmospherically corrected BRDFs. The albedo shows a spectral dependence with values in the blue band (λ = 0.472 μm) significantly and consistently higher than values at other wavelengths (λ = 0.682 and 0.870 μm). Little variation is noted from day to day except for the deep ocean case of 31 July. On this day there is a significant increase of the albedo at 0.470 μm and a decrease at all other bands. Large solar zenith angle as on 2 August, $\theta_0 \approx 44°$, seems to favor an increased albedo. The effect of the measured wind speed on the albedo is not dramatic especially if comparing cases of light winds (e.g., 23 July, 1 m s^{-1}) and strong winds (30 July, 11 m s^{-1}). The spectral influence and magnitude of whitecaps in terms of radiance augmentation is not noticeable for the range of wind speeds measured (1–11 m s^{-1}). Note that the albedo at 0.472 μm for the two cases (23 July and 2 August) should be higher than indicated because the detector saturated for some sun-glint angles. The spectral albedo ranges from 0.0408 to 0.0511 at λ = 0.472 μm and from 0.0255 to 0.0348 at

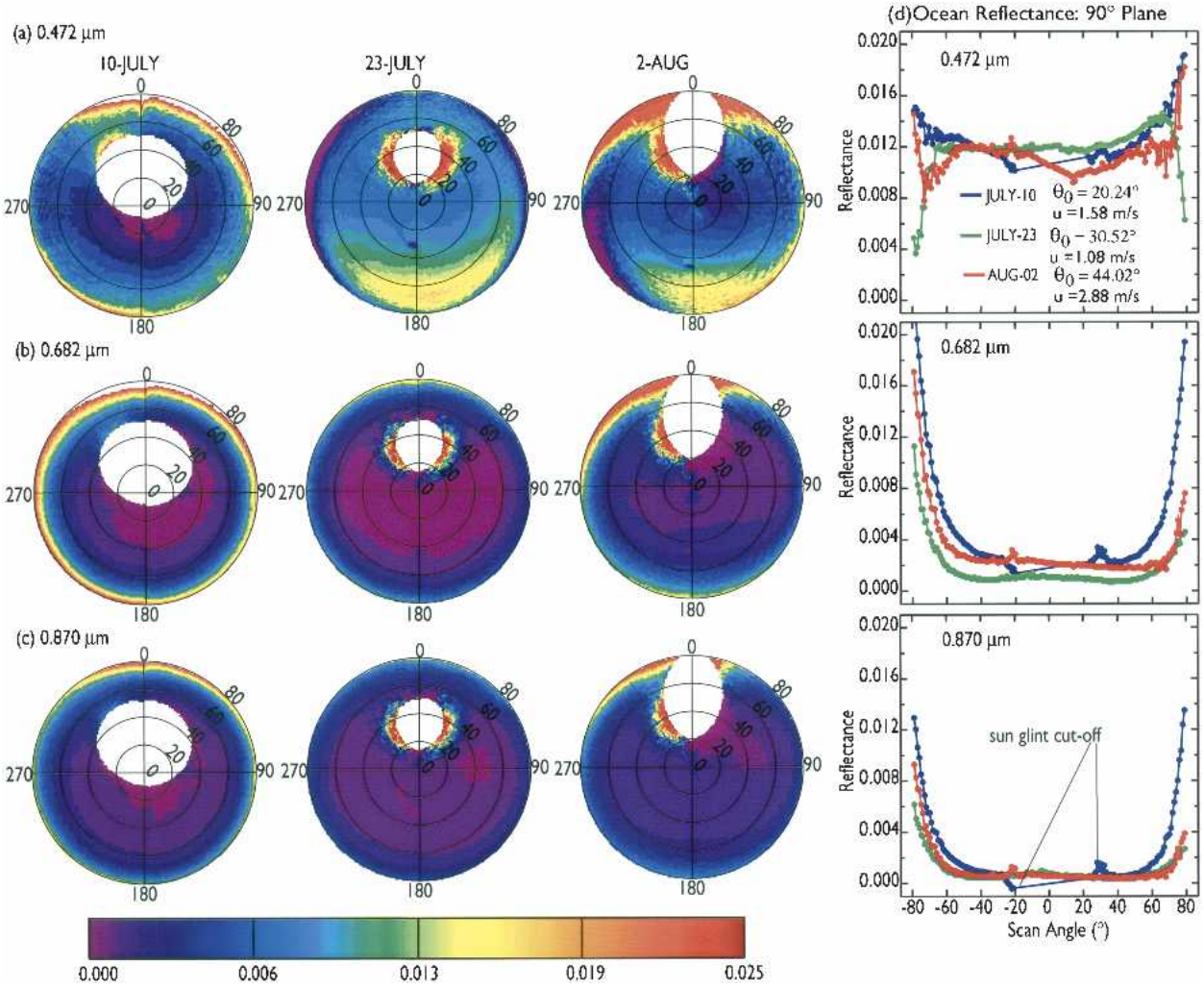

FIG. 9. Comparison of spectral BRDF for cases with low wind speeds on 10 and 23 Jul and 2 Aug at three CAR channels (0.472, 0.682, and 0.870 μm) and with the sun-glint cutoff to allow us to see more details of the variation of BRDF with view zenith angle.

$\lambda = 0.682$ μm. For near-infrared bands ($\lambda \geq 0.870$ μm), the albedo ranges from 0.0226 to 0.0309.

The albedo results are in general agreement with theoretical results of Monte Carlo simulations by Preisendorfer and Mobley (1986) where they noted little dependence of albedo on wind speed for solar zenith angles, $\theta_0 < 60°$. For small solar zenith angles the albedo increases slightly as the wind speed increases from zero, whereas for large solar zenith angles, the albedo decreases markedly as the wind speed picks up (Preisendorfer and Mobley 1986).

The equivalent water-leaving albedo values vary spectrally with high values noted in the blue band (dotted lines in Fig. 10). The values at $\lambda = 0.472$ μm ranged from 0.0098 to 0.0243; at $\lambda = 0.682$ μm the values ranged from 0.0036 to 0.0064; and for $\lambda = 0.870$ μm the values ranged from 0.0013 to 0.0038. Little variations are noted from day to day except for the deep ocean case on 31 July. On this day there is a marked increase of the equivalent water-leaving albedo at 0.470 μm and a slight decrease at all other bands. There seems to be only a small variation with respect to wind and sun angle.

e. Validation of Cox–Munk model

With the type of measurements discussed in this study, it is important to validate the widely used Cox–Munk model for predicting surface slope statistics as a function of wind speed over the ocean under the conditions we measured. Our approach involves using the Cox–Munk model to retrieve wind speed u at 10 m, separately in each band, and then use the best-fit u to compute surface reflectance that we then compare with our retrieved sun-glint BRDFs.

1) WIND SPEED RETRIEVAL

The results of the wind speed retrievals are given in the last column of Table 3. For each experiment, the

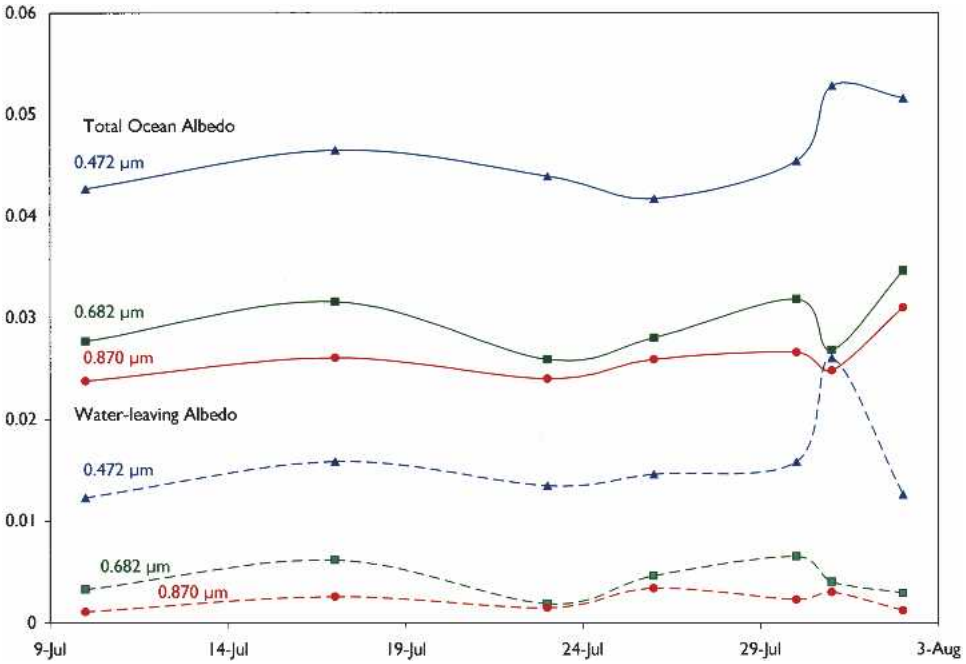

FIG. 10. Total ocean spectral albedo and average water leaving (total albedo excluding the sun glint) for seven cloud-free cases of CAR measurements over the Atlantic off the U.S. East Coast during the CLAMS field experiment campaign from 10 Jul to 2 Aug 2001. The albedo values are for $15° < \theta_0 < 45°$ and $1 \leq u$ (m s^{-1}) < 12.

lower line shows the full range over all spectral bands of the retrieved wind speed u (meters per second) associated with a height of 10 m above the sea level, and the upper line shows the in situ buoy wind speed and the measurement height. We did not apply any surface drag correction, which could change some of our results by as much as 15% (Stull 1988, 377–380).

The results show that the Cox–Munk model generally reproduces well the total reflected energy in the region of bright glint. As a result, the wind speed retrievals with our algorithm are on average unbiased. The wind speed retrievals with the modified Cox–Munk and the original Cox–Munk models produce close results for most cases and would make an interesting comparison to wind speed retrievals (for the range 3–20 m s^{-1}) from the SeaWinds Scatterometer aboard NASA's Quick Scatterometer (QuikSCAT) (Draper and Long, 2002; Freilich and Dunbar, 1999; Liu et al. 1998), if only the CAR measurements coincide with QuikSCAT overpass (~2300 UTC). The spectral dispersion of wind speed is proportional to u with a factor of 0.1–0.15, in agreement with a decrease of reflectance with an increase of wind speed.

The retrieved u values were typically close for groups of wavelengths [(0.472, 1.036, 1.219 μm) and (0.682, 0.870 μm)]. However, the latter pair of wavelengths are systematically higher by ~0.1 m s^{-1} for $u < 4$ m s^{-1}, and by about 1–4 m s^{-1} for u = 8–11 m s^{-1}. It is not clear why we have this systematic discrepancy.

In a recent study, Ebuchi and Kizu (2002) performed analysis of a large 5-yr statistical sample of the surface slope distributions derived from the geostationary radiometer in the visible wavelengths, in combination with scatterometer fields of wind speed. They found much less anisotropy and a considerably narrower distribution of slopes than those reported by Cox and Munk. The parameterizations of Nakajima and Tanaka (1983) used in our study, which is close to the original Cox–Munk slope parameterization except for low u values, allowed us to obtain a close agreement with the buoy-measured wind speeds. Similar results were obtained for Cox–Munk slope parameterization. The parameterization of Ebuchi and Kizu (2002) provides similar results at large wind speeds; however, it performs poorly at low wind speeds.

In another recent study, Su et al. (2002) reported that both the amplitude and width of the Cox–Munk model is less than that observed in measurements. This implies that the Cox–Munk model underestimates the total reflected solar energy in the bright glint region, which is different from our conclusions based on wind speed retrievals. We should mention though that such a comparison might not be relevant because the conditions of our measurements (relatively small sun angle and a rather narrow range of solar angles) were similar to the geometry of the Cox and Munk observations, whereas Su et al. (2002) conducted measurements at very large sun angles when the Cox–Munk model may not be valid.

2) ANALYSIS OF THE COX–MUNK MODEL

We focused separately on the glint regions of high ($R_{CM} > 0.02$) and low ($0.001 < R_{CM} \leq 0.02$) reflectance. The high-glint region, which is avoided in satellite ocean color remote sensing, is useful for determining the surface wind speed, atmospheric water vapor, and, potentially, aerosol single scattering albedo. The low-glint region, which may occupy a large range of angles at high wind speeds and low sun, is of great interest to the ocean color community, although the useful signal (water-leaving radiance) may be comparable to the ocean surface reflectance. For example, the current SeaWiFS algorithm masks reflectance with $R_{CM} > 0.005$ (Wang and Bailey 2001). A study by these authors based on the modified Cox–Munk model demonstrated that with the glint correction the range of ocean color retrievals can be expanded to $R_{CM} \leq 0.01$.

In their original papers, Cox and Munk (1954a, b) stated that the sensitivity of measurements was about 1000 to 1. In addition, contribution of the diffuse skylight was calculated approximately by assuming isotropic incident radiation. Given that the images were not saturated, we can assume that the range of surface reflectance that had high enough SNR, from which the slope distribution was derived, was limited to a few tenths of a percent. Thus, the lower glint region poses an additional question of accuracy for the Cox–Munk model because of limitations of instrumentation available at the time.

As mentioned earlier, we separately processed both the modified and the original Cox–Munk model with and without the Gram–Charlier expansion. The purpose of Gram–Charlier expansion as used by Cox and Munk (1954a,b) is to cause an improvement over normality assumption, because in the expansion there are parameters that directly control the skewness and kurtosis. The Cox–Munk model is incorporated in the radiative transfer code SHARM only in the direct reflected radiance, while the diffuse radiance is computed with the modified Cox–Munk model. To ensure energy conservation between the direct and diffuse radiation, the upwind (Z_x^2) and crosswind (Z_y^2) mean slopes were selected to satisfy $Z_x^2 + Z_y^2 = \sigma^2 = 0.00534u$. Cox and Munk reported that they observed the range of slope distribution anisotropy $Z_x^2/Z_y^2 = 1$–1.8 with a mean value of 1.34. In this study, we varied the value of the ratio in the range 1.34–1.50, which only insignificantly affected the wind speed retrievals and had a negligible effect on the diffuse water-leaving reflectance. Below, we present results for $Z_x^2/Z_y^2 = 1.5$ with zero offset for both upwind and crosswind components.

The results of our approximation of the high-glint region by the modified and the original Cox–Munk (without and with Gram–Charlier expansion) are shown in Fig. 11. They are given in terms of the difference between retrieved BRDF and computed reflectance (using the Cox–Munk model), normalized to the maximum retrieved spectral BRDF, to uniformly represent conditions that are different in the wind speed and solar elevation. Note that the water-leaving component is added to the computed BRDF before calculating the difference. Since the results are similar in all spectral bands and the VIS–NIR bands were saturated at low wind speeds on 23 July and 2 August, we only show the polar plots for 1.036 μm. In general, the relative accuracy of the Cox–Munk model is better than about ±30% at the CAR spatial resolution. At small wind speed (<3 m s^{-1}), the Cox–Munk model underestimates the observed reflectance in the immediate vicinity of the center of the sun glint by 3%–20%.

For low glint regions we selected three cases (26, 30, and 31 July) to show the performance of the model for both the modified Cox–Munk and the original Cox–Munk model without and with Gram–Charlier expansion (cf. Fig. 12). In general, the original Cox–Munk model performs reasonably well for the cases with medium to high wind speed (17, 26, 30, and 31 July) and poorly for the low wind speed cases (10 and 23 July and 2 August). The differences between measurements and Cox–Munk computations in this region of low reflectance range between –0.009 and 0.009. The modified Cox–Munk model shows smaller differences in all cases. It is not possible to give further analysis of the low glint region for the ocean color studies because the observation point of the radiometer varied with scan angle, and the variability we observe can be attributed to the horizontal inhomogeneity of the coastal waters. On the other hand, however, our measurements clearly show that low glint regions may pose some problems at low wind speeds.

In cases of medium and high wind speed, the original Cox–Munk model with Gram–Charlier expansion provided the better fit to the measured glint pattern than the modified Cox–Munk model, although the improvement was not dramatic (cf. Fig. 13). It also should be mentioned that even though Gram–Charlier expansion provides better fit to the measured glint pattern both in symmetry and amplitude, there still exists a small problem in asymmetry (skewness coefficient is less than 1 in all cases except 23 July and 2 August, with skewness coefficients of 1.1 and 1.7, respectively), but arguably not so significant considering the wide range of uncertainties involved as indicated earlier—experimental errors, accuracy of the radiative transfer model, uncertainty in aerosol parameters, and/or calibration errors. We certainly need larger statistics to generalize our conclusions further.

5. Summary and conclusions

The Cloud Absorption Radiometer (CAR) was flown aboard the University of Washington CV-580 research aircraft during the CLAMS field experiment where it obtained measurements of bidirectional reflec-

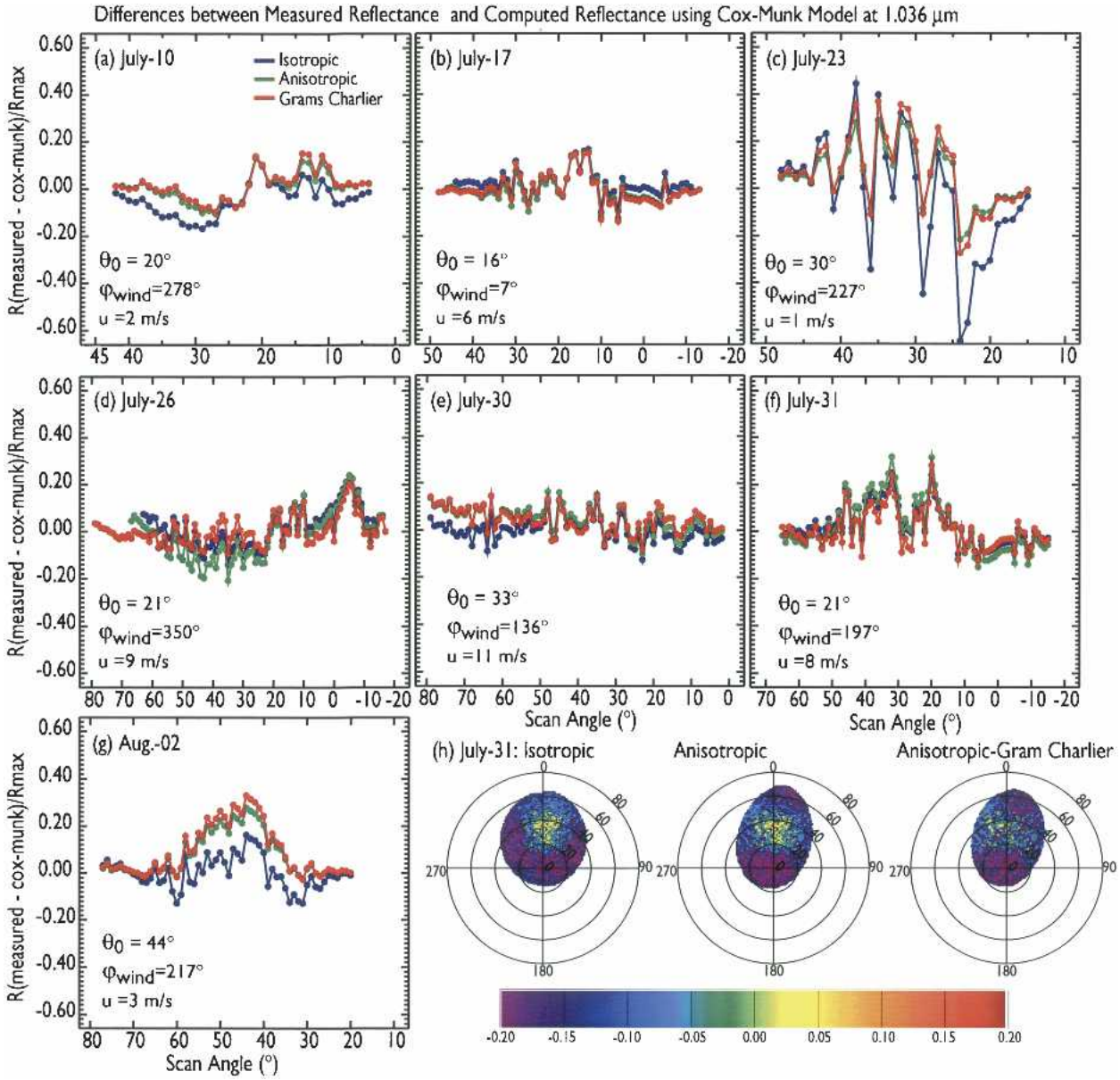

FIG. 11. (a)–(g) Normalized differences between measurements and computed reflectance using modified Cox–Munk (Nakajima and Tanaka 1983) and the original Cox–Munk (Cox and Munk 1954a,b) without and with Gram–Charlier expansion for the brightest part of the sun glint where computed reflectance $R > 0.02$. (h) The differences for the entire high glint region for 31 Jul, to serve as an illustration for the other cases.

tance distribution function (BRDF) of the ocean during July and August 2001 in conditions of high to medium sun ($15° < \theta_0 < 46°$). The measurements were accompanied by AATS-14 measurements of atmospheric aerosol and water vapor above the airplane. The properties of the total atmospheric column were evaluated from AATS-14 measurements at the lowest flight altitude (~50 m). The aerosol size distribution and refractive index were provided by analysis of nearby AERONET sun-photometer measurements at Chesapeake Light. With this ancillary information, we developed a rigorous iterative atmospheric correction algorithm that retrieves simultaneously the wind speed and full ocean BRDF (sun glint and water-leaving reflectance) from CAR measurements. The algorithm was applied to seven cloud-free days of measurements conducted over the Atlantic Ocean at the Clouds and the Earth's Radiant Energy System (CERES) Ocean Validation Experiment (COVE) EOS validation site (35.00°N, 75.68°W), and at nearby NOAA buoy stations.

The BRDF from our measurements shows the characteristic anisotropy of the water-leaving radiance, with

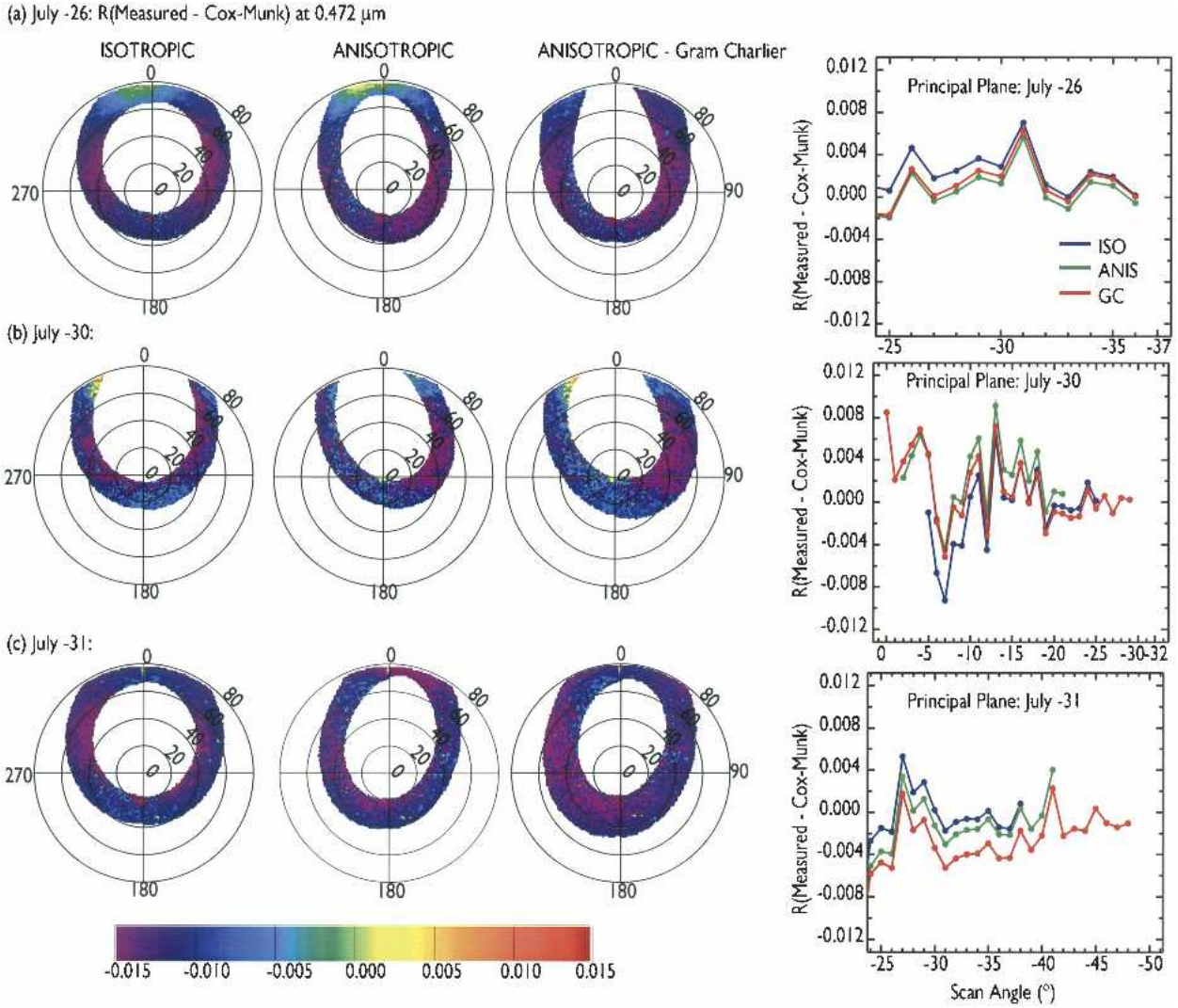

FIG. 12. Differences between measurements and computed reflectance using modified Cox–Munk (Nakajima and Tanaka 1983) and the original Cox–Munk (Cox and Munk 1954a,b) without and with Gram–Charlier expansion in the darkest part of the sun-glint reflectance ($0.001 < R < 0.02$).

increases at large view zenith angles ($\theta > 60°$), as found in simulations. This paper gives examples of the diffuse water-leaving BRDF at wavelengths of 0.472, 0.682, and 0.870 μm for different cases. This unique information is important for parameterization of ocean color algorithms for case II waters and validation analysis. We also present the water-leaving albedo and total spectral albedo of the ocean.

Results of validation of the Cox–Munk model of ocean surface reflectance show that on average the model describes well the glint pattern. As a result, the wind speed retrieved from the bright glint region with reflectance greater than 0.02 on five different cases was within ± 0.5 m s^{-1} of the in situ measurements for the range $1 < u < 11$ m s^{-1}. In the other two cases of medium wind speed ($u = 6$–8 m s^{-1}), the difference was larger (± 2.5 m s^{-1}). The retrievals of wind speed with the modified Cox–Munk model (Nakajima and Tanaka 1983), and the original Cox–Munk model with Gram–Charlier expansion (Cox and Munk 1954a,b) produced very similar results in most cases. The shape of the sun glint was reproduced on average with an accuracy of better than 30%. At low wind speeds (<2–3 m s^{-1}), the Cox–Munk model underestimates the center of the glint reflectance by about 30%. For the dark glint region with reflectance from 0.001 to 0.02, the standard deviation was on average 0.005. In cases of high wind speed, the Cox–Munk model with Gram–Charlier expansion provided the best fit.

The results of this study are an important benchmark for further work that would involve extending the observed quantitative behavior to other conditions using

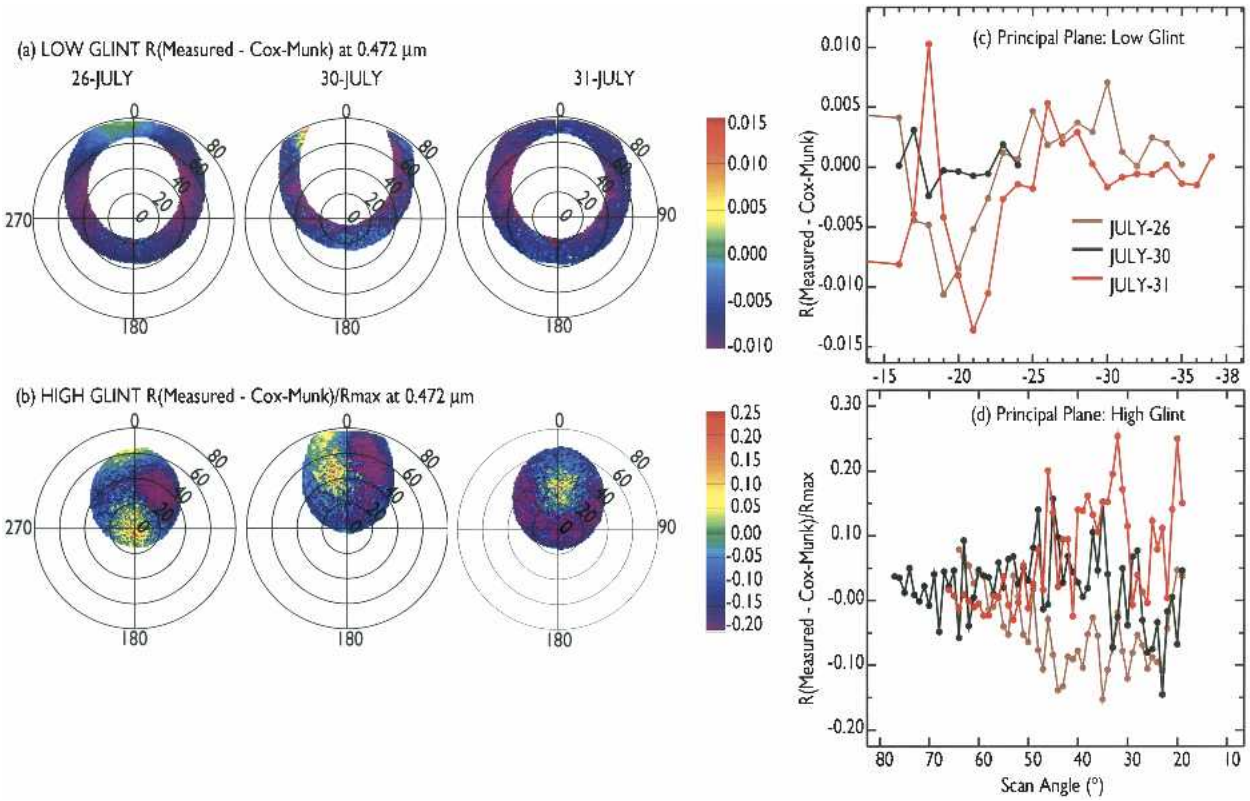

FIG. 13. Comparison of differences between measurements and computed reflectance using modified Cox–Munk (Nakajima and Tanaka 1983) for low glint and the original Cox–Munk (Cox and Munk 1954a,b) with Gram–Charlier expansion for three cases (26, 30, and 31 Jul) with the strongest wind (8–11 m s^{-1}).

other analytical models and radiative transfer (RT) simulations of an ocean–atmosphere system. It is also possible to combine our measured albedo and solutions of RT with climatological values of wind speed and water type to generate a detailed atlas of the albedos over the oceans. The recent availability of comprehensive ocean–atmosphere datasets makes such calculations feasible. However, such a project, worthwhile as it is, is beyond the scope of the present paper.

Acknowledgments. The authors are especially grateful to P. V. Hobbs and the University of Washington CV-580 staff members for great assistance in data collection. Thanks also to P. K. Shu, H. H. Jones, and team for engineering support. We express our appreciation for graphics support to R. B. Simmon and J. E. Schmaltz (Fig. 1); B. Napper, J. A. O'Leary, K. A. Gammage, and C. L. Ladd (Fig. 2); and J. Riédi for his support of Mgraph software. We also acknowledge size distribution data derived from AERONET sunphotometer measurements at Chesapeake Light Tower and wind information from NOAA buoy stations. This research was supported by funding provided by NASA's Radiation Science Program, the MODIS Science Team, and the EOS Project Science Office. The study was conducted as part of Chesapeake Lighthouse and Aircraft Measurements for Satellites (CLAMS) experiment. We are grateful to the CLAMS science team, especially W. L. Smith and T. P. Charlock, for their support in coordination and planning of the field campaign.

REFERENCES

Cox, C., and W. Munk, 1954a: The measurements of the roughness of the sea surface from photographs of the sun's glitter. *J. Opt. Soc. Amer.,* **44,** 838–850.

——, and ——, 1954b: Statistics of the sea surface derived from sun glitter. *J. Mar. Res.,* **13,** 198–227.

——, and ——, 1955: Some problems in optical oceanography. *J. Mar. Res.,* **14,** 63–78.

Draper, W. W., and D. G. Long, 2002: An assessment of SeaWinds on QuikSCAT wind retrieval. *J. Geophys. Res.,* **107,** 3212, doi:10.1029/2002JC001330.

Dubovik, O., B. N. Holben, T. F. Eck, A. Smirnov, Y. J. Kaufman, M. D. King, D. Tanré, and I. Slutsker, 2002: Variability of absorption and optical properties of key aerosol types observed in worldwide locations. *J. Atmos. Sci.,* **59,** 590–608.

Duntley, S. Q., 1954: Measurements of the distribution of water wave slopes. *J. Opt. Soc. Amer.,* **44,** 574–575.

Ebuchi, N., and S. Kizu, 2002: Probability distribution of surface wave slope derived using sun glitter images from Geostationary Meteorological Satellite and surface vector winds from scatterometers. *J. Oceanogr.,* **58,** 477–486.

Fougnie, B., R. Frouin, P. Lecomte, and P. Y. Deschamps, 1999: Reduction of sky-light reflection effects in the above-water

measurements of diffuse marine reflectance. *Appl. Opt.,* **38,** 3844–3856.

Freilich, M. H., and R. S. Dunbar, 1999: The accuracy of the NSCAT 1 vector winds: Comparisons with National Data Buoy Center buoys. *J. Geophys. Res.,* **104,** 11 231–11 246.

Gatebe, C. K., M. D. King, S. Platnick, G. T. Arnold, E. F. Vermote, and B. Schmid, 2003: Airborne spectral measurements of surface-atmosphere anisotropy for several surfaces and ecosystems over southern Africa. *J. Geophys. Res.,* **108,** 8489, doi:10.1029/2002JD002397.

Gordon, H. R., 1997: Atmospheric correction of ocean color imagery in the Earth Observing System era. *J. Geophys. Res.,* **102,** 17 081–17 106.

——, and M. H. Wang, 1994: Retrieval of water-leaving radiance and aerosol-optical thickness over the oceans with SeaWiFS—A preliminary algorithm. *Appl. Opt.,* **33,** 443–452.

Guinn, A. J., Jr., G. N. Plass, and W. Kattawar, 1979: Sunlight glitter on a wind-ruffled sea: Further studies. *Appl. Opt.,* **18,** 842–849.

Hale, G. M., and M. R. Querry, 1973: Optical constants of water in the 200 nm to 200 μm wavelength region. *Appl. Opt.,* **12,** 555–563.

Hooker, S. B., and C. R. McClain, 2000: The calibration and validation of SeaWiFS data. *Progress in Oceanography,* Vol. 45, Pergamon, 427–465.

——, G. Lazin, G. Zibordi, and S. McLean, 2002: An evaluation of above- and in-water methods for determining water-leaving radiances. *J. Atmos. Oceanic Technol.,* **19,** 486–515.

Hulburt, E. O., 1934: The polarization of light at sea. *J. Opt. Soc. Amer.,* **24,** 35–42.

Kaufman, Y. J., J. V. Martins, L. A. Remer, M. R. Schoeberl, and M. A. Yamasoe, 2002: Retrieval of black carbon absorption from proposed satellite measurements over the ocean glint. *Geophys. Res. Lett.,* **29,** 1928, doi:10.1029/2002GL015403.

Kleidman, R. G., Y. J. Kaufman, B. C. Gao, L. A. Remer, V. G. Brackett, R. A. Ferrare, E. V. Browell, and S. Ismail, 2000: Remote sensing of total precipitable water vapor in the near-IR over ocean glint. *Geophys. Res. Lett.,* **27,** 2657–2660.

King, M. D., M. G. Strange, P. Leone, and L. R. Blaine, 1986: Multi-wavelength scanning radiometer for airborne measurements of scattered radiation within clouds. *J. Atmos. Oceanic Technol.,* **3,** 513–522.

Liu, W. T., W. Q. Tang, and P. S. Polito, 1998: NASA Scatterometer provides global ocean-surface wind fields with more structures than numerical weather prediction. *Geophys. Res. Lett.,* **25,** 761–764.

Loisel, H., and A. Morel, 2001: Non-isotropy of the upward radiance field in typical coastal (Case II) waters. *Int. J. Remote Sens.,* **22,** 275–295.

Lyapustin, A., and T. Z. Muldashev, 1999: Method of spherical harmonics in the radiative transfer problem with non-Lambertian surface. *J. Quant. Spectrosc. Radiat. Transfer,* **61,** 545–555.

——, and ——, 2000: Generalization of Marshak boundary condition for non-Lambert reflection. *J. Quant. Spectrosc. Radiat. Transfer,* **67,** 457–464.

Morel, A., 1988: Optical modeling of the upper ocean in relation to its biogenous matter content (case-I waters). *J. Geophys. Res.,* **93,** 10 749–10 768.

——, and B. Gentili, 1993: Diffuse reflectance of oceanic waters. II. Bidirectional aspects. *Appl. Opt.,* **32,** 6864–6879.

——, and ——, 1996: Diffuse reflectance of oceanic waters. III. Implication of bidirectionality for the remote-sensing problem. *Appl. Opt.,* **35,** 4850–4862.

——, K. J. Voss, and B. Gentili, 1995: Bidirectional reflectance of oceanic waters: A comparison of modeled and measured upward radiance fields. *J. Geophys. Res.,* **100,** 13 143–13 150.

——, D. Antoine, and B. Gentili, 2002: Bidirectional reflectance of oceanic waters: Accounting for Raman emission and varying particle scattering phase function. *Appl. Opt.,* **41,** 6289–6306.

Mueller, J. L., and R. W. Austin, 1995: Ocean optics protocol for SeaWiFS validation, revision 1. NASA Tech. Memo 104566, Vol. 25, NASA Goddard Space Flight Center, 66 pp.

Nakajima, T., and M. Tanaka, 1983: Effect of wind-generated waves on the transfer of solar radiation in the atmosphere–ocean system. *J. Quant. Spectrosc. Radiat. Transfer,* **29,** 521–537.

Preisendorfer, R. W., and C. D. Mobley, 1986: Albedos and glitter patterns of a wind-roughened sea surface. *J. Phys. Oceanogr.,* **16,** 1293–1316.

Redemann, J., and Coauthors, 2005: Suborbital measurements of spectral aerosol optical depth and its variability at subsatellite grid scales in support of CLAMS, 2001. *J. Atmos. Sci.,* **62,** 993–1007.

Rothman, L. S., and Coauthors, 2003: The HITRAN molecular spectroscopic database: Edition of 2000 including updates through 2001. *J. Quant. Spectrosc. Radiat. Transfer,* **82,** 5–44.

Soulen, P. F., M. D. King, S.-C. Tsay, G. T. Arnold, and J. Y. Li, 2000: Airborne spectral measurements of surface–atmosphere anisotropy during the SCAR-A, Kuwait oil fire, and TARFOX experiments. *J. Geophys. Res.,* **105,** 10 203–10 218.

Schooley, A. H., 1954: A simple optical method for measuring the statistical distribution of water surface slopes. *J. Opt. Soc. Amer.,* **44,** 37–40.

Stull, R. B., 1988: *An Introduction to Boundary Layer Meteorology.* Kluwer Academic, 666 pp.

Su, W., T. P. Charlock, and K. Rutledge, 2002: Observations of reflectance distribution around sunglint from a coastal ocean platform. *Appl. Opt.,* **41,** 7369–7383.

Voss, K. J., 1989: Electro-optic camera system for measurement of the underwater radiance distribution. *Opt. Eng.,* **28,** 241–247.

Walker, R. E., 1994: *Marine Light Field Statistics.* John Wiley & Sons, 675 pp.

Wang, M. H., and S. W. Bailey, 2001: Correction of sun glint contamination on the SeaWiFS ocean and atmosphere products. *Appl. Opt.,* **40,** 4790–4798.

Yan, B., K. Stamnes, M. Toratani, W. Li, and J. J. Stamnes, 2002: Evaluation of a reflectance model used in the SeaWiFS ocean color algorithm: Implications for chlorophyll concentration retrievals. *Appl. Opt.,* **20,** 6243–6259.

Yang, H., and H. R. Gordon, 1997: Remote sensing of ocean color: Assessment of water-leaving radiance bidirectional effects on atmospheric diffuse transmittance. *Appl. Opt.,* **36,** 7887–7897.

Zhao, F., and T. Nakajima, 1997: Simultaneous determination of water-leaving reflectance and aerosol optical thickness from Coastal Zone Color Scanner measurements. *Appl. Opt.,* **36,** 6949–6956.

Zibordi, G., S. B. Hooker, J. F. Berthon, and D. D'Alimonte, 2002: Autonomous above-water radiance measurements from an offshore platform: A field assessment experiment. *J. Atmos. Oceanic Technol.,* **19,** 808–819.